Temporal reconstruction and transfer of the source term in computational hybrid aeroacoustics for low Mach numbers

T.M. Hylkema

TU Delft Delft University of Technology

Challenge the future

Temporal reconstruction and transfer of the source term in computational hybrid aeroacoustics for low Mach numbers

by

T.M. Hylkema

in partial fulfillment of the requirements for the degree of

Master of Science
in Aerospace Engineering

at the Delft University of Technology,
to be defended publicly on Monday April 30, 2018 at 10:00 AM.

Supervisor:	Dr. ir. A.H. van Zuijlen,	TU Delft
Thesis committee:	Dr. ir. M.I. Gerritsma,	TU Delft
	Dr. F. Avallone,	TU Delft

TU Delft Delft University of Technology

Summary

In this research two acoustic analogies, the linearized Euler equations and Lighthill's equation are evaluated. These equations describe the propagation of acoustic waves. Both the linearized Euler equations and Lighthill's equation use a right hand side source term that is determined by a fluid solver. When coupling the fluid solver with an acoustic solver for a low Mach number aeroacoustic problem, a difference in spatial and temporal scale can exist for the fluid and acoustic calculations. This research is based on aeroacoustic solvers in which the spatial grid for the acoustics and the fluid is exactly the same. Due to this condition it is shown that the ratio between the fluid and acoustic time step is governed by the inverse of the Mach number to ensure that both the Courant and acoustic Courant numbers are smaller than one. In the case of low Mach numbers ($M < 0.1$) this results in a time step difference between the acoustic and fluid simulation of at least a factor 10. Due to the time step difference, the source term in the fluid solver is not updated for every acoustic time step and hence the accuracy of the acoustic result is reduced. To remedy this decreased accuracy one could solve for the source term at every acoustic time step. However this leads to lengthy computations. The objective of this research is thus to improve the efficiency of the fluid acoustic coupling by increasing the acoustic accuracy for non-matching time steps in the fluid solver and in the acoustic solver. This research objective can be fulfilled by improving the source term transfer from the acoustic solver to the fluid solver by higher order temporal interpolation between different source levels. Furthermore the source term can be reconstructed at the nodes by implementation of a higher order time integration method in the fluid solver. In this research is investigated whether the improved temporal transfer and reconstruction of the source term can lead to an increased time step difference between the fluid and acoustic calculations for which an acceptable acoustic accuracy can be obtained.

The approach taken in this research is based on firstly quantifying the effect of keeping an analytic monopole source term constant for multiple acoustic time steps. To adequately describe how the source term is updated, a source term Courant number is derived. This number is defined as the time interval between source term updates multiplied by the summation of the convective velocity and the speed of sound and divided by the spatial acoustic step. Then the source term levels are interpolated with Lagrange polynomials, to assess the improvement of the acoustic results. Furthermore this known analytic monopole source term is reconstructed by solving an ordinary differential equation that has the monopole as its exact solution. Both the spectral deferred correction method and the backward Euler method are used to solve this equation. The spectral deferred correction method is a higher order method that uses iterative low order substepping over Gauss Lobatto quadrature nodes. Using Gauss Lobatto quadrature allows for exact integration of the integral in the Picard formulation. In the last part of this research the spectral deferred correction method is implemented in an incompressible, transient fluid solver to construct higher order source terms. Lagrange interpolation is used to interpolate the source terms at the Gauss Lobatto node locations, to improve the source term transfer to the acoustic solver.

The results from this research show that a large distortion of the acoustic results take place when the source term Courant number exceeds one. For the source term transfer to the acoustic solver, interpolation with Lagrange basis functions over Gauss Lobatto nodes delivered the most accurate acoustic results. In terms of higher order time integration, the reconstruction of the source term by solving an ordinary differential equation with the spectral deferred correction method showed the highest accuracy. The root-mean-square error of the acoustic result was decreased compared to a backward Euler method. The relative effect on the improvement of the acoustic accuracy proved to be highest by Lagrange interpolation over the Gauss Lobatto nodes compared to accuracy improvements at the nodes by the spectral deferred correction method. Finally based on the result from the implementation of the spectral deferred correction method in the incompressible, transient fluid solver, it can be noted that the spectral deferred correction method did not show the same error convergence as was found in the solution of an ordinary differential equation for the reconstruction of the analytic monopole. The

Lagrange interpolation over the Gauss Lobatto node locations improved the overall acoustic result in the active source region of the flow. In the far field the acoustic results were similar for both zeroth order interpolation (which resembles the original piecewise constant source term) and Lagrange interpolation.

Acknowledgements

I would like to thank my supervisor, Sander van Zuijlen, for his guidance. I enjoyed our meetings and discussions, which progressed my research and thinking every time.

Finally I would like to thank my family and friends for their support. In particular I would like to thank my mother, Annika, for supporting me every step of the way.

Contents

List of abbreviations

BE	Backward Euler
FE	Forward Euler
FFT	Fast Fourier transform
LES	Large eddy simulation
LEE	Linearized Euler equations
ODE	Ordinary differential equation
PISO	Pressure implicit splitting operations
PPW	Points per wavelength
RHS	Right hand side
RMS	Root-mean-square
SDC	Spectral deferred correction
SPL	Sound pressure level

List of symbols

Greek symbols

γ	specific heat ratio
δ_{ij}	Kronecker delta
ϵ	error
λ	wavelength
ν	kinematic viscosity
ρ	density
σ	viscous stress tensor

Roman symbols

c_0	speed of sound
f	frequency
l	Lagrange multiplier
M	Mach number
P	compressive stress tensor
p	pressure
Q	spectral integration matrix
r	residual
S	node to node spectral integration matrix
s	spectral quadrature weight
T	Lighthill's turbulent stress tensor
t	time
t_a	acoustic time step
t_f	fluid time step
t_s	source term update time step
u	velocity
x	location

1

Introduction

In the last 25 years large strides have been made in the development of computational aeroacoustic methods. In the early nineties of the 20th century the problem was classified as a very premature research area [1]. Today, noise quantification is a major design consideration [2]. Due to the advancement of research in computational aeroacoustics, noise can be quantified in a preliminary stage in the design process. This leads to more noise efficient prototypes and end-products. Furthermore it prevents modifications late in the design process. Applications that benefit specifically from a low aerodynamic noise footprint are wind turbine blades that are operated in the vicinity of populated areas. Another application of aeroacoustics can be found in the aircraft industry, where both the acoustic quantification inside the aircraft and in the far-field is an important topic.

In general, aeroacoustics describes the interaction between an acoustics field and a flow field. It describes the origination and propagation of sound waves that are created by aerodynamic sources. Many challenges are associated with this process. The acoustic waves have often a significantly different propagation velocity than the convective velocity of the fluid. Furthermore the spatial length of the smallest turbulent flow structures that create the acoustic waves can be considerably lower than the acoustic wavelengths [1]. Generally the acoustic field has a larger domain than the fluid domain, and acoustic values are often required at a significant distance away from the source. The need for fundamentally different time and space scales and a large computational domain thus asks for an optimal use of the available computational resources.

Sound is quantified by deviations from the mean pressure level in air. The perturbations can be determined by solving the compressible Navier-Stokes equations. As was stated different characteristic time and space scales are needed to be solved for the acoustic variables. In order to avoid divergence of the acoustic and flow simulations the finest grid and time scale are then required in a direct method. This causes lengthy calculations. In order to adhere to the acoustic and flow Courant constraints in an efficient manner, hybrid methods are developed. In hybrid methods the flow is calculated in a source region. The source is used as a right hand side in the acoustic equations. Extensive research is conducted in the development of hybrid methods. The non-linear source term in the acoustic wave equation that describes the acoustics propagation, originates from turbulent fluid behaviour [3] [4]. The implementation of a hybrid method requires a solution for the different temporal and spatial scales for flow and acoustics.

In a decoupled, hybrid approach a computational cheap addition to solving the fluid is found by incorporating the acoustics. In this research the same mesh is used for the fluid calculation and the acoustic calculation, which prevents the need for higher order solvers in space for the acoustics. However this causes a difference in required time scale between the acoustic and the fluid calculations. The objective is to find a time step ratio between the fluid and the acoustics, which is as high as possible, since this reduces the computational load. The acoustic time step is held constant throughout this research. The aim is thus to increase the fluid time step, while still achieving a high accuracy. To achieve a higher ratio between the fluid time step and the acoustic time step, two methodologies are used, i.e.

temporal source term reconstruction (higher order time integration) and temporal source term transfer (Lagrange interpolation). This research is focused on the effect of time integration and interpolation in the fluid solver to improve the acoustic calculations in an efficient manner. Summarizing, the following research goals can be defined:

- Quantify the acoustic error for various time steps at which the source term is updated, while maintaining a constant number of acoustic time steps.
- Find an improved temporal source term transfer to the acoustic solver by implementing higher order temporal source term interpolation to increase the maximum ratio of the fluid and acoustic time step.
- Create an improved temporal reconstruction of the source term by higher order time integration in the fluid solver to increase the maximum ratio of the fluid and acoustic time step.
- Establish the relative effect of the temporal transfer of the source term (interpolation) and the temporal reconstruction of the source term (higher order time integration) on reduction of the acoustic error for disparate time scales in the hybrid aeroacoustic system.

This research thus aims to find a generalized source term reconstruction and transfer methodology that improves the efficiency of the hybrid system. The main research question is: can the efficiency of the coupling between a fluid solver and an acoustic solver benefit from temporal interpolation and/or higher order temporal source term reconstruction?

Chapter 2 describes the underlying physics of computational hybrid aeroacoustics. Two important acoustic analogies, Lighthill's acoustic analogy and the linearized Euler equations are treated here. Then in Chapter 3 an analytic source term is used to establish a research hypothesis. In this chapter the effect of keeping the source term constant for multiple acoustic time steps is tested. The effect on the acoustic results is monitored. A relation to the acoustic Courant number is established. Based on this research hypothesis, Chapter 5 investigates interpolation strategies to interpolate the fluid results, as a way to improve source term transfer to the acoustic solver. Furthermore in this chapter a higher order time integration scheme, the spectral deferred correction method, is assessed. Both the interpolation technique and the time integration method are used to reconstruct the monopole source term, to assess improvements in acoustic results. Finally Chapter 5 considers the implementation of the spectral deferred correction method and the interpolation technique in a fluid solver, to reconstruct the source term in a quasi-direct approach. In this context, quasi-direct, means that the source term is only saved for the amount of substeps during one fluid time step.

2

Physics behind computational aeroacoustics

A large part of this research is focused on a mathematical assessment of temporal source term characterization. This chapter treats the more physical background of aeroacoustics and the underlying assumptions for establishing the acoustic analogies, with the acoustic wave propagation on the left hand side of the equation and the source term definition on the right hand side. Before assessing the effect of keeping a source term constant over multiple acoustic time steps and applying the higher order source term reconstruction and transfer, this chapter treats some fundamental theory underlying computational aeraocoustics. It serves as an introduction to the research presented in Chapters 3, 4 and 5.

2.1. Introduction

The fundamental theory discussed in this chapter first consists of a qualitative assessment of the mechanism of sound, i.e.: sound origination, sound transmission and sound reception. Then a mathematical description of sound is given by discussing and deriving two acoustic equations from the Navier-Stokes equations which are based on distinct underlying assumptions. These acoustic wave equations with an aerodynamic source term are: Lighthill's acoustic analogy and the linearized Euler Equations (LEE). Although a multitude of acoustic analogies exist, these analogies are arguably the most well-known. Finally a research framework is constructed of the current challenges in constructing an aerodynamic source term to solve the acoustic equations accurately and efficiently.

2.2. Mechanism of sound

As shown in Figure 2.1, acoustics can be divided in three main phases: origination, transmission and reception. In this section these three areas are addressed.

2.2.1. Sound origination

The research area of aeroacoustics describes the acoustic wave propagation created by air flows, which is a fundamentally different process than sound generated by vibrating solid objects. According to Lighthill [5], experiments have shown that the frequencies that exist in the flow are identical to the frequency of the sound waves. The challenge is to quantify the intensity of sound, which is determined by the part of the energy of the flow that is converted to acoustic energy. The acoustic energy causes longitudinal transverse fluctuations of air molecules that are perceived as sound.

In Figure 2.2 a schematic image is shown of a flow over an airfoil. The interaction between the airfoil and the flow causes an acoustic field which is propagating in all directions. The sound waves are characterized by a sinusoidal variations in amplitude. The sound wave is described by the amplitude,

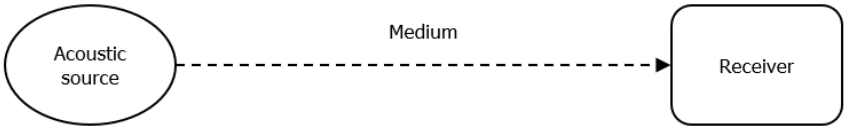

Figure 2.1: Phases within acoustics.

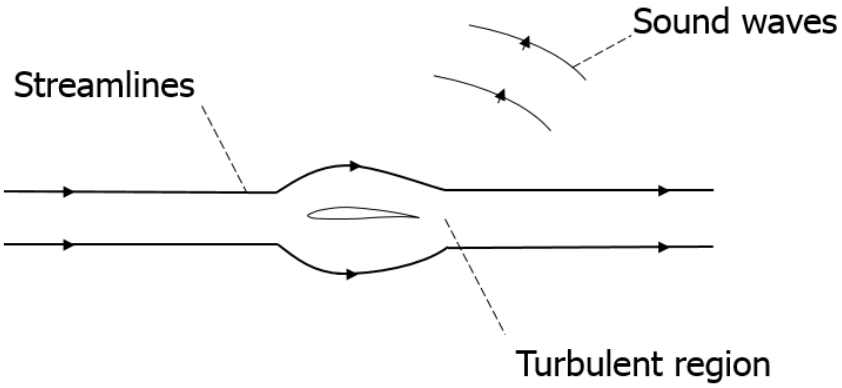

Figure 2.2: Sound waves created by the turbulent region in the airflow.

frequency and propagating speed. The relation between the propagating speed (speed of sound), $c_0(m/s)$, the wavelength $\lambda(m)$ and the frequency, $f(Hz)$ is defined as:

$$f = \frac{c_0}{\lambda}. \tag{2.1}$$

In the boundary layer of an airflow, instabilities can occur which are amplified. These instabilities interact with one another causing a turbulent flow. The inertial behaviour of the flow particles are counteracted by the viscosity of the fluid, this balance is enclosed in the Reynolds number. If the Reynolds number is high the disturbance propagates in a large amount of frequencies. For lower Reynolds numbers the growth rate of the instabilities is less and also the range of frequencies in which they propagate. Furthermore sound can be amplified by the existence of obstacles in the flow. Some obstacles can work as a resonator, by oscillating at specific frequencies. The specific frequencies are then amplified, which creates a characteristic sound. [1]

Aerodynamic sound is characterized by small pressure perturbations in air, and is thus an inherently unsteady phenomenon. There are three fundamental source terms that describe the origination of sound. These elementary source terms are known as: monopoles, dipoles and quadrupoles. A monopole resembles a mass or heat injection in the fluid. Dipoles originate from pressure fluctuations at walls[6]. Finally fluctuations can be induced by viscous stress in the flow or non-isentropic effects. The instabilities in the viscous shear layer propagate in an unsteady manner and cause pressure fluctuations from the mean pressure value that are perceived as sound. Mathematically this effect is described by

[1] Lecture on Aerodynamic Generation of Sound, by James Lighthill & John Ffwocs Williams (source: YouTube)

a quadrupole.

2.2.2. Sound propagation

The sound can be influenced by the medium through which it is propagated. Acoustic waves can have low amplitude and long wavelengths compared to the airflow and propagate at the speed of sound. In this research a one way coupling between flow and acoustics is assumed. This means that only the effect of flow on the acoustics is addressed. In the medium reflection (by objects) and refraction effects can occur, which requires the need for sufficient boundary conditions in order to accurately describe the acoustic field [1].

In a medium refraction effects can occur, due to the the existence of a structure. This structure can cause large pressure differences in the flow, leading to an unstable boundary layer in which fluctuations create turbulent elements (eddies). The fluctuations can have a certain frequency which is based on the length of the fluctuations and the convection speed of the flow ($f = U/L$). These fluctuations cause acoustic waves. The wavelength of these acoustic waves are thus related to the length of the fluid elements and the ratio of the speed of sound and the convective velocity. This will be treated more extensively in Chapter 3. In the case of low Mach numbers, the ratio between the speed of sound and the convective velocity, $\frac{1}{M}$, is high. This means that the typical difference in length scale between the acoustic wavelength and the length of the flow element is large. This then poses a challenge for acoustic numerical implementation [7].

2.2.3. Sound reception

Sound is perceived by excitations of the ear drum. These excitations occur due to deviations from the mean pressure. Sound is thus inherently unsteady. As a way to quantify sound the root-mean-square value of sound is often used:

$$\tilde{p} = \sqrt{(\bar{p'^2})}. \tag{2.2}$$

Although the physiology of the ear is not discussed in detail in this report, the general threshold of hearing is 10^{-5} Pa and the maximum acoustic signal strength that the human ear can bear is 10^{2} Pa [8]. The sound pressure level, shown in Equation 2.3 is calculated by using an international reference value. This reference value is the minimum sound pressure level which the ear can experience for a $2kHz$ sinusoidal signal. And corresponds to a value of $10^{-5}Pa$. The sound pressure level is expressed as

$$SPL = 10log(\frac{\tilde{p}}{p_{ref}})^2. \tag{2.3}$$

Here the sound pressure level is expressed in decibels (dB). In order to characterize sound a distinction needs to be made between the acoustic particle velocity, which determines the strength of the acoustic signal and the propagation speed of the sound waves in a medium. The acoustic propagation is determined by the speed of sound. In terms of frequency sound can be perceived in the range of 16 Hz up to 2000 Hz [8].

To quantify sound both the frequency of the signal and the strength of the signal need to be addressed. The relation between the signal strength and the frequency is given by the power spectral density. The power spectral density describes the signal intensity for the entire frequency range of sound.

2.3. Governing Equations

So far a qualitative description of sound is given. In this section the aerodynamic origination and propagation of sound is mathematically described by deriving and discussing Lighthill's acoustic analogy and the linearized Euler equations. These are two fundamentally different approaches of describing both

sound propagation and sound origination that use different assumptions and have therefore different applications.

2.3.1. Lighthill's acoustic analogy

Lighthill's acoustic analogy is arguably the most famous equation describing sound origination from an aerodynamic source and wave propagation in a stationary medium. It is a wave equation that is rewritten from the Navier-Stokes equations. This inhomogeneous wave equation describes sound sources and the propagation of sound. The sound that is described is caused by a turbulent flow as was qualitatively described in the previous section. The objective of the equation is to describe the acoustic waves in the far field, as opposed to determining the acoustics in the flow region. Lighthill's equation is based on the exact conservation equations of a fluid and does not make any compressibility assumptions in the region of turbulence [7].

Lighthill's equation can be derived from the conservation equations for mass and momentum [5]. Below the derivation of Lighthill's equation is described. First take the time derivative of the continuity equation:

$$\frac{\partial}{\partial t}(\frac{\partial}{\partial t}(\rho) + \frac{\partial}{\partial x_i}(\rho u_i)) = 0. \tag{2.4}$$

Furthermore take the spatial derivative of the momentum equation, where only body forces are excluded,

$$\frac{\partial}{\partial x}(\frac{\partial}{\partial t}(\rho u_i) + \frac{\partial}{\partial x_j}(\rho u_i u_j + P_{ij})) = 0. \tag{2.5}$$

Now, subtract Equation 2.4 from Equation 2.5, which results in:

$$\frac{\delta^2}{\delta t^2}(\rho) = \frac{\delta^2}{\delta x_i \delta x_j}(\rho u_i u_j + P_{ij}), \tag{2.6}$$

where P_{ij} is the compressive stress tensor acting on a portion of the fluid [5], defined by

$$P_{ij} = (p - p_\infty)\delta_{ij} - \sigma_{ij}, \tag{2.7}$$

with p_∞ the ambient pressure and σ_{ij} the viscous stress tensor. The density is written as a fluctuation from the mean density, since these are the variables of interest in an acoustic context:

$$\rho' = \rho - \rho_\infty. \tag{2.8}$$

Next subtract the expression $\frac{\partial^2}{\partial {x_i}^2}(\rho' {c_\infty}^2)$ from Equation 2.6 to obtain:

$$\frac{\partial^2 \rho'}{\partial t^2} - c_0^2 \frac{\partial^2 \rho'}{\partial x_i \partial x_i} = \frac{\partial^2 T_{ij}}{\partial x_i \partial x_j}. \tag{2.9}$$

This then results in Equation 2.9. Note that c_∞ is the ambient speed of sound in the stationary propagation medium. To find this equation the following relation is used:

$$\frac{\partial \rho'}{\partial t} = \frac{\partial \rho}{\partial t}. \tag{2.10}$$

This approach is valid since the waves are propagating in a stationary medium. Equation 2.9 represents Lighthill's acoustic analogy. On the right hand side it shows the source term whereas on the left hand side it contains the propagation variables.

The term T_{ij},

$$T_{ij} = \rho u_i u_j + (p' - c_0^2 \rho')\delta_{ij} - \sigma_{ij}, \tag{2.11}$$

represents the instantaneous applied stress in any point in the fluid[9] [5].

The density and pressure perturbations are respectively defined as $\rho - \rho_\infty$ and $p - p_\infty$. Myamoto [10] describes that in the case of adiabatic flow and a sufficiently high Reynolds number, the source term can be reduced to $T_{ij} = \rho u_i u_j$. This means that the source term can be solved by an incompressible solver. The density perturbation ρ' is shown as part of the wave function on the left hand side, that simulates wave propagation. Here c_0 represents the free stream speed of sound. As was stated in the introduction to this chapter, the propagation medium is assumed to be a homogeneous medium at rest [9]. It can be noted that the assumption of a homogeneous medium at rest is not applicable for determining the source term. Lighthill's acoustic analogy can therefore only be used outside the source region.

The left side of the equation 2.9 shows the propagation of the acoustic waves in a stationary medium at the speed of sound. The right side is the source term that includes all effects that create acoustic waves. Lighthill's equation thus supplies an analogy for the acoustic wave propagation as a result from turbulent flow in a finite volume region. A crucial part of Lighthill's equation is that the speed of sound is based on the stationary medium and not on the flow region where compressibility effects can occur that severely change the value of the speed of sound. The sole objective of Lighthill's equation is thus to establish the acoustic waves that propagate away from the source region. The source term thus determines the way that fluid perturbations are coupled with the propagation of sound waves in the far field. As opposed to linear acoustics no approximations in the source region are made. In linear acoustics non-linear interactions and viscous effect are neglected. The aspects that are not covered by the linearized acoustic equations are included on the right hand side source term in Lighthill's acoustic analogy [7].

2.3.2. Linearized Euler Equations

The previous section showed the equation for sound generation based on Lighthill's acoustic analogy. As was touched upon Lighthill's acoustic analogy uses different assumptions compared to the linearized Euler equations. The main difference can be explained by the objective of both acoustic equations. The linearized Euler equations can be used to determine the acoustic waves inside the flow. Whereas Lighthill's acoustic analogy is used to determine noise in the far field only. However, Lighthill is an exact derivation from the Navier-Stokes equations, taking all aerodynamic effects that cause acoustic waves into account. Although the source region can be determined exactly by Lighthill's acoustic analogy, it assumes that the sound is radiated in free space and that due to the assumption of homogeneity of the propagating medium, no sound can be determined inside the source region. The linearized Euler equations are created by a linearization of the wave equation, thus neglecting non-linear turbulent terms and neglecting viscous effects.

In this section the aeraocoustic equations are derived from the Navier-Stokes equations. From these equations the linearized Euler equations are derived and insight is given in the justification of the underlying assumptions. As was stated the linearized Euler equation assume isentropic and inviscid flow. Thus there is no heat conduction and the entropy remains constant. Due to the fact that the linearized Euler equations assume that fluctuations are propagated linearly the eddies remain coherent structures [7].

Derivation of the LEE

In this section the aeroacoustic equations are derived from the Navier-Stokes equations, which are given by

$$\frac{\partial \rho}{\partial t} + \frac{\partial}{\partial x_i}(\rho u_i) = S_c \tag{2.12a}$$

$$\frac{\partial \rho u_i}{\partial t} + \frac{\partial}{\partial x_i}((\rho u_i u_j) + p\delta_{ij} - \sigma_{ij}) = S_{m,i} \tag{2.12b}$$

$$\frac{\partial \rho e_t}{\partial t} + \frac{\partial}{\partial x_i}(\rho e_t u_i + p u_i - u_j \sigma_{ij} + q_j) = S_e. \tag{2.12c}$$

Here ρ represents the density, u the velocity, σ the viscous stress tensor, and e_t the total energy [8]. The right hand side source terms of the conservation equations are described by S_c, $S_{m,i}$ and S_e.

As was stated before, the acoustics are described by pressure perturbations. Thus the conservation equations need to be expressed in terms of pressure and velocity perturbations. To do so the velocity and pressure can be decomposed in a mean value and a fluctuating value:

$$u = u_0 + u' \tag{2.13a}$$

$$p = p_0 + p'. \tag{2.13b}$$

The pressure fluctuations are very small compared to the mean pressure, therefore multiplications of perturbations can be left out of the equation (compare the threshold of hearing and pain, 10^{-5} Pa and 10^2 Pa respectively, with the ambient pressure of 10^5 Pa). Furthermore the absence of viscous effects can be assumed, since viscosity has very little effect on acoustic propagation. Therefore the propagation of sound waves is assumed to be isentropic, which means that the density equation becomes redundant. The Navier-Stokes equations are thus transferred in to the linearized Euler equations. Finally the mean density is normalized. Therefore the following system of equations remains according to [11],

$$\frac{\partial u_i'}{\partial t} + \frac{\partial}{\partial x_j}(u_i' u_{0j} + p') + \frac{\partial u_{0i}}{\partial x_j}(u_j' + \frac{p'}{\gamma p_0} u_{0j}) = S_{m,i} \tag{2.14a}$$

$$\frac{\partial p'}{\partial t} + \frac{\partial}{\partial x_i}(\gamma p_0 u_i' + p' u_{0i}) + (\gamma - 1)(p' \frac{\partial u_{0i}}{\partial x_i} - u_i' \frac{\partial p_0}{\partial x_i}) = S_e \tag{2.14b}$$

which is showing on the left side the propagation effects and on the right side the source terms that are inserted externally. The system is left the same as in [11] in order to compare acoustic results for different source term reconstructions later in the research. In this equation γ represents the ratio of specific heats. Furthermore it can be noted that the value of p' is determined with respect with the mean pressure of the flow whereas in Lighthill's equation p' is determined with the stationary (mean) pressure. [7] The source term formulation for the linearized Euler equations is based on a derivation by Bogey, Bailly and Juvé [3], which is

$$S_{m,i} = -\frac{\partial \rho u_i' u_j'}{\partial x_j} \tag{2.15a}$$

$$\overline{S_{m,i}} = -\overline{\frac{\partial \rho u_i' u_j'}{\partial x_j}}. \tag{2.15b}$$

According to Bogey, Bailly and Juvé [3] the source terms are only non-linear in the velocity perturbations. The velocity field that is calculated by a CFD solver can thus be used to construct the source terms. Based on the analysis of both Lighthill's acoustic analogy and the linearized Euler equations, the application of these acoustic equations can be summarized by Figure 2.3.

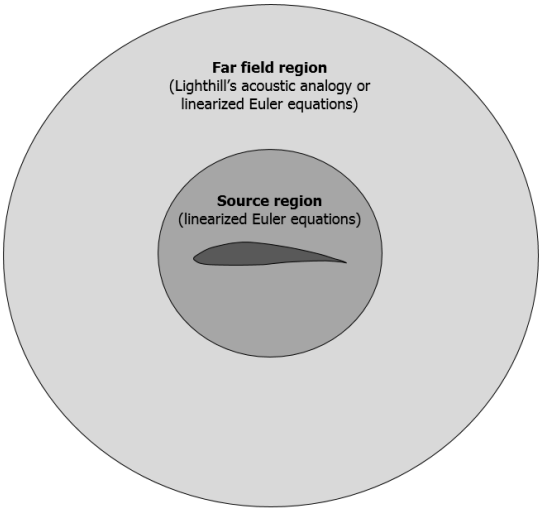

Figure 2.3: Different regions in computational domain flow and applicability of acoustic equations.

2.4. Challenges in CAA research

The main objective of this research is to incorporate an improved hybrid aeroacoustic system for low Mach number flow cases. So far some of the physics behind aeroacoustics have been qualitatively and mathematically described. Furthermore two important acoustic equations, Lighthill's acoustic analogy and the linearized Euler equations, have been addressed which are used throughout this research.

In computational hybrid aeroacoustics sources are computed by a flow solver. This flow solver calculates the acoustic effects of the turbulent dynamics of the source region. The acoustic effects are contained in the source term of the wave equations, which then needs to be solved for the acoustic propagation variables on the left hand side of the equation [4].

To avoid lengthy computations by using a direct method, the hybrid approach allows for determining the source region on a smaller domain. A large difference in fundamental length scales for the acoustic and fluid length scales can exist. To connect different length scales interpolation approaches need to be developed. However, in this research no spatial interpolation is used. The same spatial grid for both the fluid and the acoustics is used. However, a fundamental difference in characteristic time scales can occur. As was elaborated on in this chapter, the frequency of the source terms is the same as the acoustics frequency. However the propagating velocity of the sound waves is different than the convective velocity of a low Mach number fluid flow. This asks for a time interpolation approach to make sure that the source term which is calculated by the flow solver can be accurately described in an efficient way. Furthermore by implementing a higher order time integration scheme, a higher order solution in time can be computed to increase the accuracy of the solution. The acoustic field is sensitive to any form of perturbation it is thus crucial to describe the acoustic source term in an accurate way, which is the main challenge of this research.

3

Acoustic quantification of source term transfer

3.1. Introduction

When making a coupling between a fluid solver and an acoustic solver for a specific aeroacoustic problem, a difference in spatial and temporal scale can exist. In this chapter tests are conducted for an aeroacoustic solver in which the spatial grid for the acoustics and the flow is exactly the same. Depending on the type of problem, this can result in a difference between time scales between the flow solver and the acoustics solver.

Acoustic waves travel at the speed of sound ($u_\infty \approx 343 m/s$ [7], in air depending on local conditions), whereas low Mach number flows have a convective velocity that is at least a factor ten slower ($M < 0.1$). Since the mesh for the acoustic calculations is the same as the mesh for the flow calculations, this imposes a condition on the ratio of time scales between both solvers. In order to determine a suitable time step the acoustic and flow Courant number have to be taken into account. The flow Courant number is defined as:

$$\textit{Courant number} = \frac{u\Delta t_f}{\Delta x_f}. \tag{3.1}$$

Here u is the flow velocity (m/s), Δt_f is the time step (s) and Δx_f is the spatial step in the fluid solver. The acoustic Courant number is defined as:

$$\textit{acoustic Courant number} = \frac{(u + c_0)\Delta t_a}{\Delta x_a}. \tag{3.2}$$

Here Δt_a represents the time step (s) in the acoustic solver, Δx_a the spatial step (m) in the acoustic solver and c_0 represents the speed of sound (m/s). Since the Mach number is defined as $M = u/c_0$, Equation 3.2 can be rewritten to:

$$\textit{acoustic Courant number} = (1 + M)\frac{c_0\Delta t_a}{\Delta x_a}. \tag{3.3}$$

In general one could say (depending on the chosen discretization and solution methodology) that in order to obtain an accurate representation of the convective transport and the wave propagation the flow Courant and acoustic Courant numbers should not exceed one. Since this research focuses on low Mach numbers, $u << c_0$, Equation 3.1 and 3.2 can be rewritten to:

$$\frac{u\Delta t_f}{\Delta x_f} = \frac{(c_0)\Delta t_a}{\Delta x_a} = 1. \tag{3.4}$$

Equation 3.4 can be further rewritten to:

$$\frac{u}{c_0}\frac{\Delta x_a}{\Delta x_f}\frac{\Delta t_f}{\Delta t_a} = 1. \tag{3.5}$$

This means that if the same grid is used for both the acoustics and for the flow simulations ($\Delta x_f = \Delta x_a$) the following equation remains:

$$\frac{u}{c_0}\frac{\Delta t_f}{\Delta t_a} = 1. \tag{3.6}$$

The Mach number is defined as:

$$M = \frac{u}{c_0}. \tag{3.7}$$

Thus combining Equation 3.6 and 3.7 leads to the following condition:

$$M = \frac{\Delta t_a}{\Delta t_f}. \tag{3.8}$$

Based on equation 3.8 the ratio between acoustic time step and fluid time step is governed by the Mach number. To avoid divergence of the solution, the time steps have to differ at least a factor ten for low Mach number flows ($M < 0.1$) when using the same spatial grid. The acoustic calculations thus require a finer temporal discretization than the flow calculations. The acoustic field is essentially a by-product from the fluid calculation, the main computational effort is centered at the source term calculation, i.e. the fluid solution. Thus employing many smaller acoustic time steps does not have a major influence on the total computational expense of the hybrid solver. Also due to the fact that the acoustic solver is using the same spatial grid as the fluid, the acoustic solver does not have to use high order wave preserving spatial discretization and solution methodologies.

The general objective of this research is to find an improved solver coupling that allows for larger differences in time step between the flow simulation and the acoustic simulation when using the same spatial grid. By having larger disparate time scales while still attaining a sufficient level of accuracy increases the efficiency of the hybrid solver. This chapter aims to quantify the effect of discretization of a source term, i.e. the source term is held constant at fixed intervals. Based on the research objective one could define a third type Courant number, which is defined as

$$\textit{source term Courant number} = \frac{\Delta t_s}{\Delta x_a} \cdot (u + c_0). \tag{3.9}$$

Here t_s defines the time between source term updates, Δx_a the acoustic spatial step size, u the convective velocity and c_0 the speed of sound. This generalized Courant number combines the acoustic and fluid parameters to give an expression for the convergence condition of a hybrid aeroacoustic system. This source term Courant number is thus solely concerned with the coupling of the system. It can be noted that whenever the acoustic solver is coupled to a fluid solver, t_s is similar to the fluid time step t_f (when assuming that at every fluid time step a source term is calculated).

The difference in the acoustic result is quantified by means of the root-mean-square error that is computed by the difference between a distorted source term and a source term that updates at every acoustic time step.

In this chapter the effect of the ratio of flow and acoustic time step is quantified. In this chapter not a flow solver is coupled to the acoustics solver, but an analytically defined monopole source term is used.

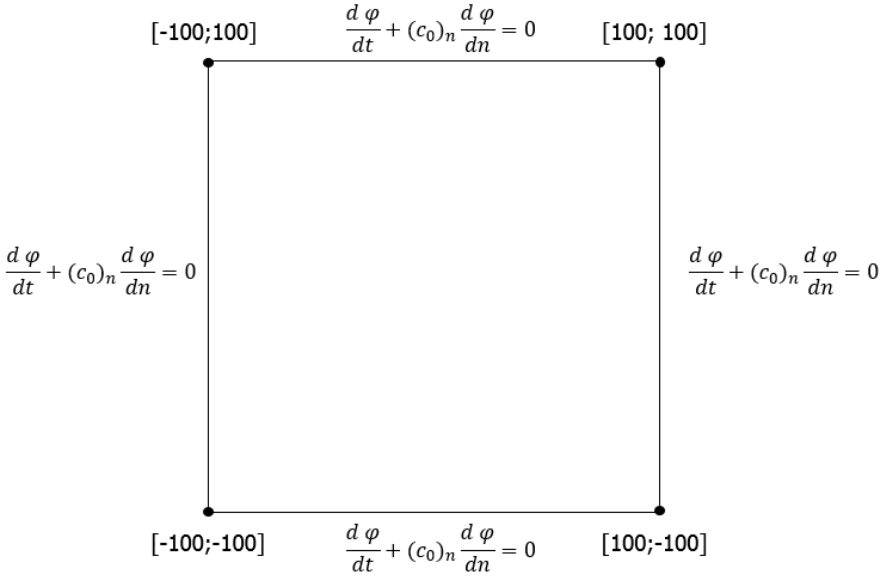

Figure 3.1: Overview of the acoustic domain. The dimensions of the domain are shown at the corners. Along the sides of the domain the convective outlet boundary condition is shown. Here φ is a generalized variable and is replaced for $u'_{i,j}$, p' or ρ'. The speed of sound, c_0, is evaluated with respect to its normal direction.

This provides the opportunity to efficiently assess the effect of different time scale ratios between the source term updates and the acoustic time steps. The acoustic error is measured as a function of the source term Courant number. Since the spatial and temporal discretization is not altered, the source term update time step t_s is the only parameter that is causing a change in the source term Courant number. Based on the quantification of the signal distortion due to different source term updates a research hypothesis is formulated.

3.2. Source term formulation

The acoustic source term connects the flow to the acoustics [11]. The acoustic source term and the propagation of the acoustics can be formulated in multiple ways, based on the number of assumptions that are made, like refraction effects and non-homogenity of the flow. In this chapter an implementation of the linearized Euler equations is used to analyze acoustic behaviour that is excited by a source term. The derivation of the Linearized Euler Equations from the Navier Stokes equations was shown in Chapter 2. In this chapter a Riemann solver is used to solve the linearized Euler equations. This solver is second order accurate in space [11]. It uses a 4-stage Runge Kutta scheme to march in time. The boundary conditions need to be non-reflective in order to prevent contamination of the acoustic domain. Therefore the convectiveOutlet boundary condition is used, which is an already implemented boundary condition in OpenFOAM. It solves the convective equation at the boundary for the unknown variables to provide an outflow of the waves from the acoustic domain. An overview of the domain and its boundary conditions can be found in Figure 3.1.

The functionality of this solver is tested by using a monopole to excite the system. A monopole is a harmonic pulsating sphere [12]. It resembles a mass injection in the continuity equation and heat addition in the energy equation. The flow in this test is assumed to be isentropic, which makes the monopole only a source term in the energy equation. The formula of the monopole is defined as:

$$S_i = \epsilon \cdot sin(\omega t) \cdot e^{-\alpha(x^2+y^2)}. \tag{3.10}$$

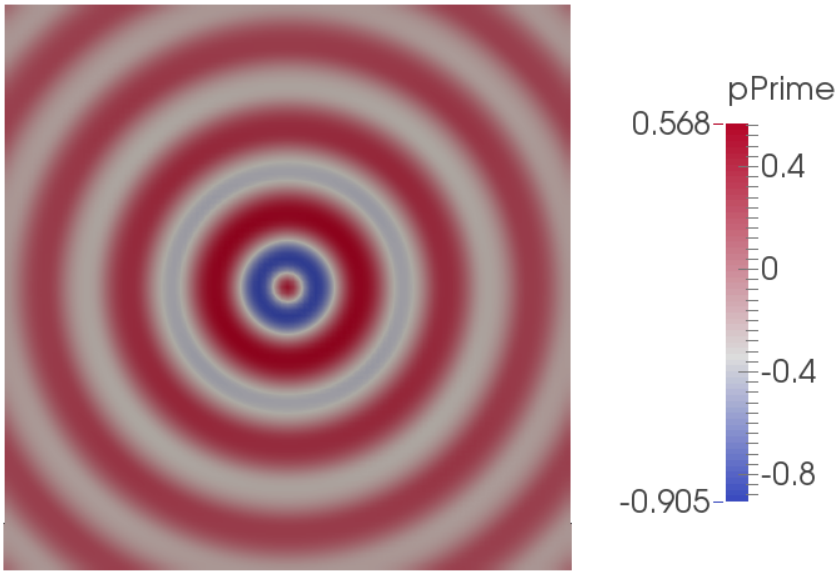

Figure 3.2: Pressure perturbation at $t = 150s$ with a $100X100$ structured grid and a 4-stage Runge Kutta time integration scheme.

In Equation 3.10 ϵ resembles the amplitude of the harmonically pulsating source term, ω is the radial frequency and α is a measure for the source decay. The source is applied in the entire acoustic domain.

3.3. Test case set-up

The acoustic source is discretized by a number of time steps. The acoustic results are then evaluated to quantify the acoustic decay for various sampling ratios. A visual example of the source term updates can be found in Figures 3.3-3.5. From these figures it can be noted that the acoustic time step is held constant, whereas the source term updates are varied. The analytical source term is used as an analogy to the output from a flow solver.

The time step used in the acoustic solver equals $0.125s$. Furhermore a stepsize of $2m$ is used and a speed of sound of $1m/s$. The flow is stationary and uniform, so $u = 0m/s$. Based on Equation 3.2 this resembles an acoustic Courant number of 0.0625. The waves propagate during $150s$. An image of

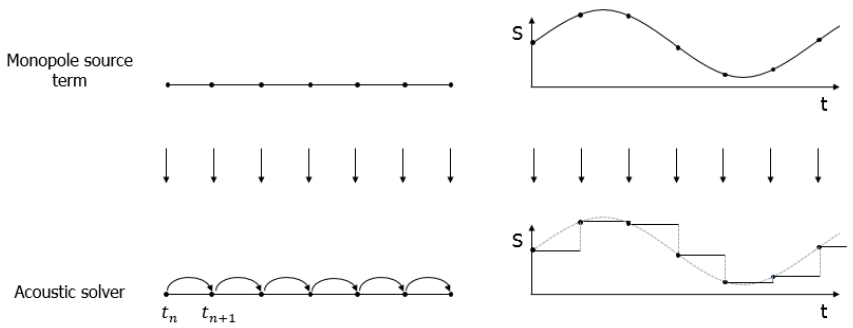

Figure 3.3: Source term update at each acoustic time step.

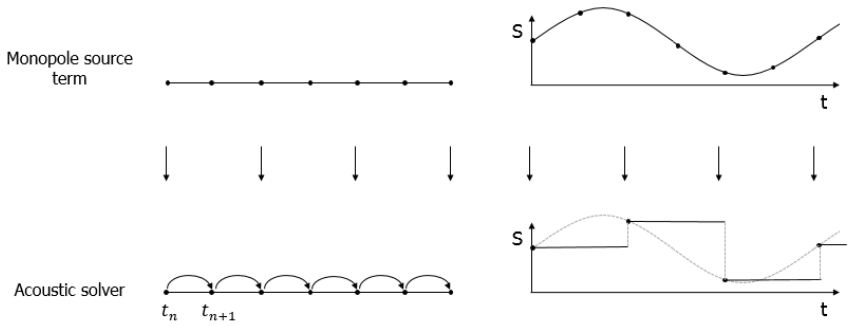

Figure 3.4: Source term update at every 2 acoustic time steps.

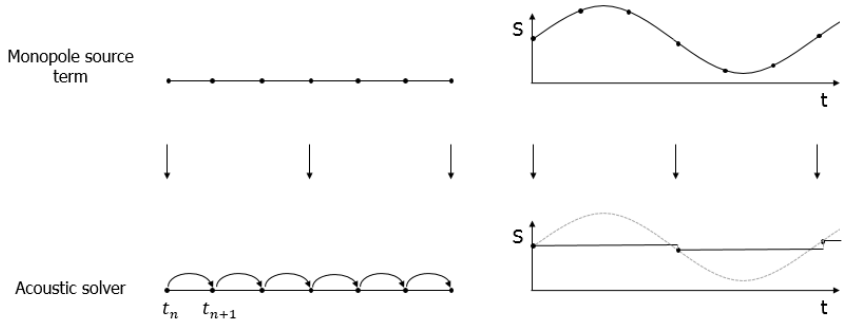

Figure 3.5: Source term update at every 3 acoustic time steps.

the wave propagation as a result of the monopole excitation can be viewed in Figure 3.2. The source term, as shown in Equation 3.10, is sampled at different time steps. Finally the monopole parameters as described in Section 3.2 are $\alpha = ln(2)/9$, $\omega = 0.2094$ and $\epsilon = 1$. Finally the monopole is excited in a stationary medium, so $u = 0$.

In Figure 3.6 A $400X400$ mesh is used as spatial discretization. The acoustic propagation is given along the center line of the domain. This solution is nearly similar to the analytical solution based on a free space Green's function [13] [14].

The propagation of the acoustic waves is considered along a $100X100$ mesh, which decreases the run time of the solver. Solving the acoustic variables over this mesh takes approximately 15 minutes, extending the simulation to a $400X400$ grid thus leads to a run time of around 4 hours. Based on a significant amount of planned tests, a $100X100$ mesh is used for the testing phase. The results are shown in Figure 3.7. From this figure it can be noted that the $400X400$ monopole has higher accuracy, specifically along the center of the domain. However in order to assess the results of different time integration approaches a $100X100$ mesh will be sufficient. This enhances the efficiency of the test schedule.

3.4. Monopole excitation results

The source term, which is dictated by the monopole equation can be varied, by keeping the monopole constant for several acoustic time steps. Initially the values of the monopole source term are sampled at $t = 0.125s$, which is at every time step in the acoustic solver. The source term Courant number is then the same as the acoustic Courant number, which is 0.0625. By keeping the acoustic time step the same and changing the time at which the source gets updated a distortion of the acoustic results is to be expected. Multiple ratios of source term sampling are tested. First the source term is held

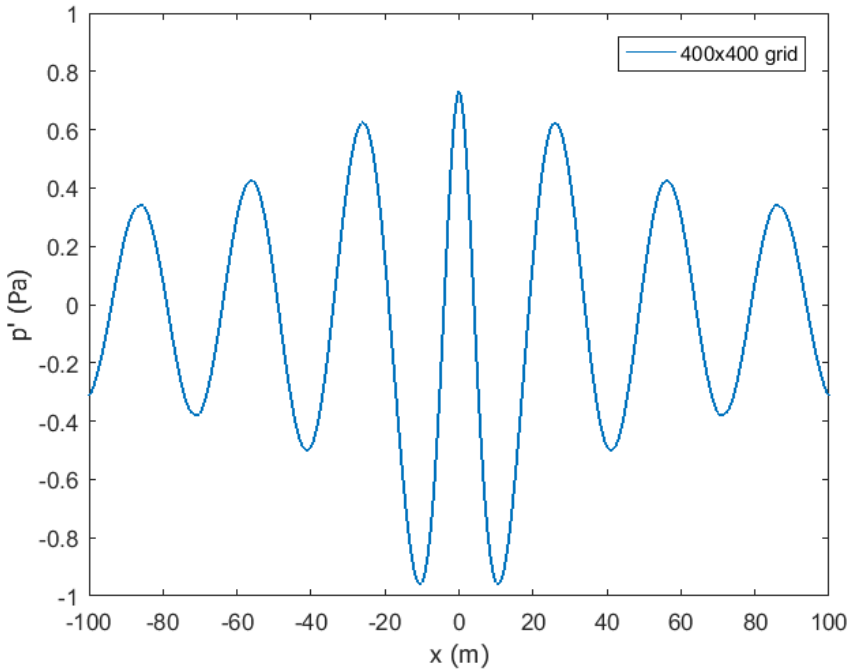

Figure 3.6: Perturbed pressure along centerline of domain at $t = 150s$ (excitation by a monopole).

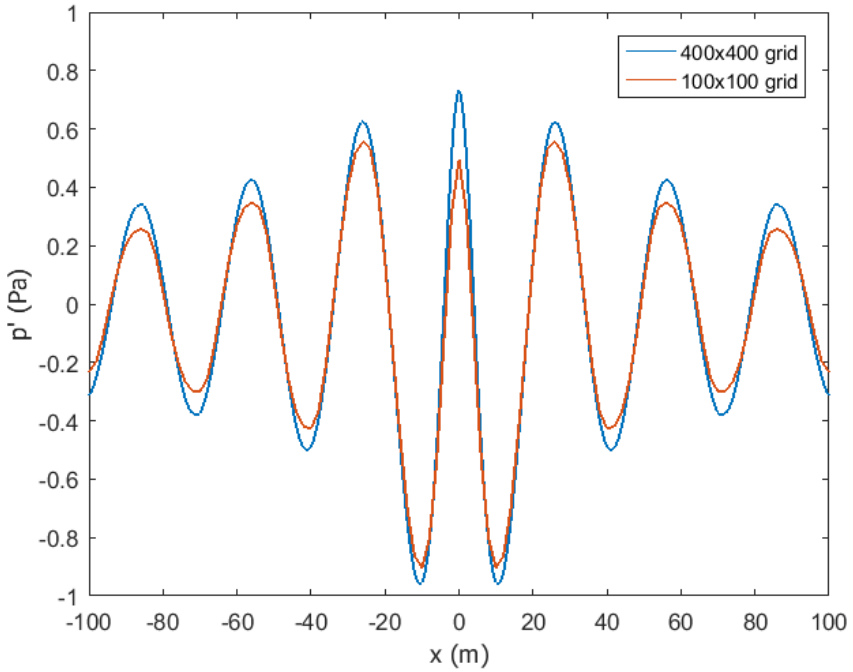

Figure 3.7: Perturbed pressure along centerline at $t = 150s$ (excitation by a monopole).

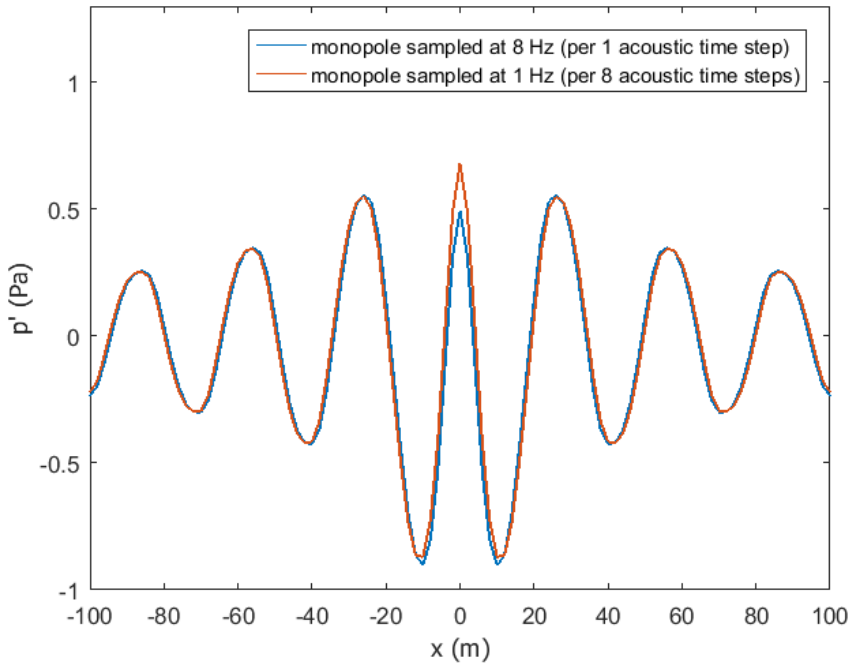

Figure 3.8: Perturbed pressure along centerline at $t = 150s$ (excitation by a monopole).

constant every $1s$, which means that after 8 acoustic time steps the source term gets updated. Basically the acoustic solver is progressed along 8 acoustic steps, while using the same value of the source term. Since the source term is held constant over these values, this resembles a piecewise constant function. This experiment is then repeated for 16, 32, 64, 128 and 256 times the acoustic time step. The acoustic solver uses a 4th order explicit Runge Kutta scheme, which is maintained during the tests.

Figure 3.8 shows the perturbed pressure over the horizontal centerline of the acoustic domain. It can be noted that a discretization of 8 times an acoustic time step still gives a good resemblance compared to a sampling at every acoustic timestep. The main difference can be noted at the center of domain, which seems to move slighthly out of phase, compared to the exact solution.

From Figure 3.9 the piecewise constant time interval is increased to $16s$, which resembles a source term Courant number equal to 1. It can be noted that deviations in the perturbed pressure increase. Again at the middle of the centerline, where the monopole is excited there is a phase difference. This is due to the fact that the monopole is updating every $2s$, whereas in the original solution the monopole is updating every $0.125s$. Furthermore the red line, is moving out of phase over the entire centerline, meaning it is running slower than the original solution. The phase difference in the center around $x = 0$ can be explained by the fact that the monopole is updated at different times, but should not affect the rest of the solution. The source term is updated at the right hand side of the sampling interval, by rounding the remainder of a division to the nearest multiple of the divider. So if the source term is updated every $8s$, this means that at an acoustic time of $t_a = 17s$, the source term time, $t_s = 24s$, is used for the acoustic solution. Mathematically this can be summarized as a piecewise constant interval of the source term,

$$t_n < t \leq t_{n+1}, \tag{3.11}$$

where the source term is then updated as

$$S(x,t) = S(x,t_{n+1}). \tag{3.12}$$

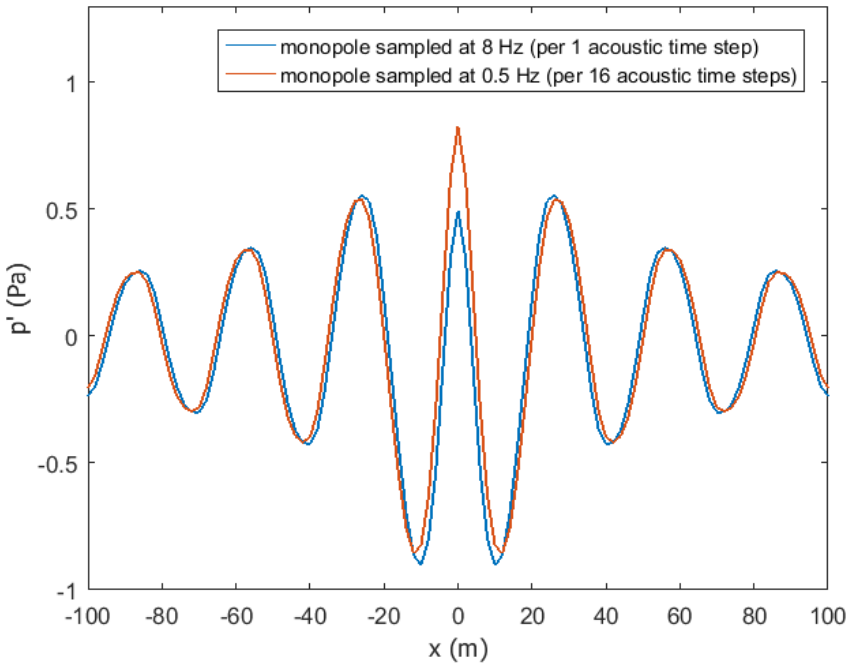

Figure 3.9: Perturbed pressure along centerline at $t = 150s$ (excitation by a monopole).

By taking the right hand side of the piecewise constant domain the source term update is leading compared to the original monopole in which an update of the monopole is determined at every acoustic time step. This thus results in a perturbed pressure that is leading the reference solution. From Figure 3.9 it can be noted that this is indeed the case.

However over the entire domain one would expect that the solver produces results that are in phase. In Figure 3.9 it can be noted that this result starts deviating from the reference solution.

In Figure 3.10 the degradation of the signal can be noted. Not only are the acoustic waves running out of phase, also the amplitude of the signal is smaller than the reference solution. Figure 3.11 shows a similar image as Figure 3.10, but the degradation of the results in terms of dispersion and dissipation is even worse. A source term update every $2s$ and a source term update every $4s$ gives a significantly different result than a source term update between, $4s$ and $8s$.

In Figure 3.12 the results are degrading even more. Now the amplitude is higher than the exact solution. Again the monopole is moving out of phase at the center point of the middle line. From Figure 3.13 it can be noted that the signal has decayed entirely. The source term is updated every $32s$, which exceeds the temporal wavelength of the harmonizing monopole point source (which is $30s$ for an angular velocity of $\omega = 0.2094$. This means that the PPW (points per wavelength) is less than one which explains the lack of accuracy of this result.

In Figure 3.14 the root-mean-square error is plotted as a function of the number of time steps that are held constant during the sampling of the source term. The root-mean-square error is defined according to Equation 3.13. For $p'_{reference}$ the solution along the centerline is taken from the $100X100$ structured grid with a 8 Hz sampling ratio (source update at every aoustic time step, for $\Delta t = 0.125s$).

$$\textit{root-mean-square error} = \sqrt{\frac{\sum_{i=1}^{n}((p'_i - p'_{i,reference})^2)}{n}} \tag{3.13}$$

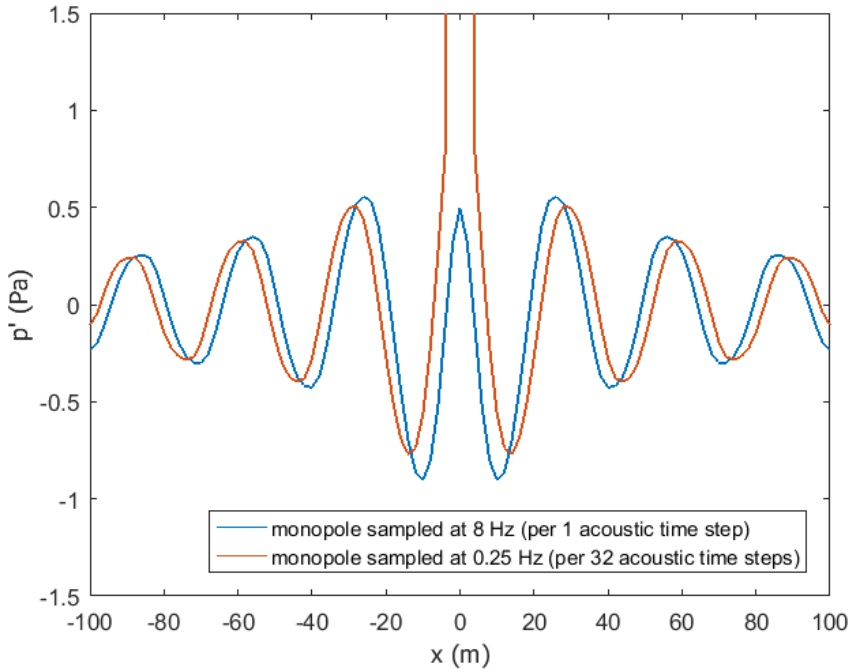

Figure 3.10: Perturbed pressure along centerline at $t = 150s$ (excitation by a monopole).

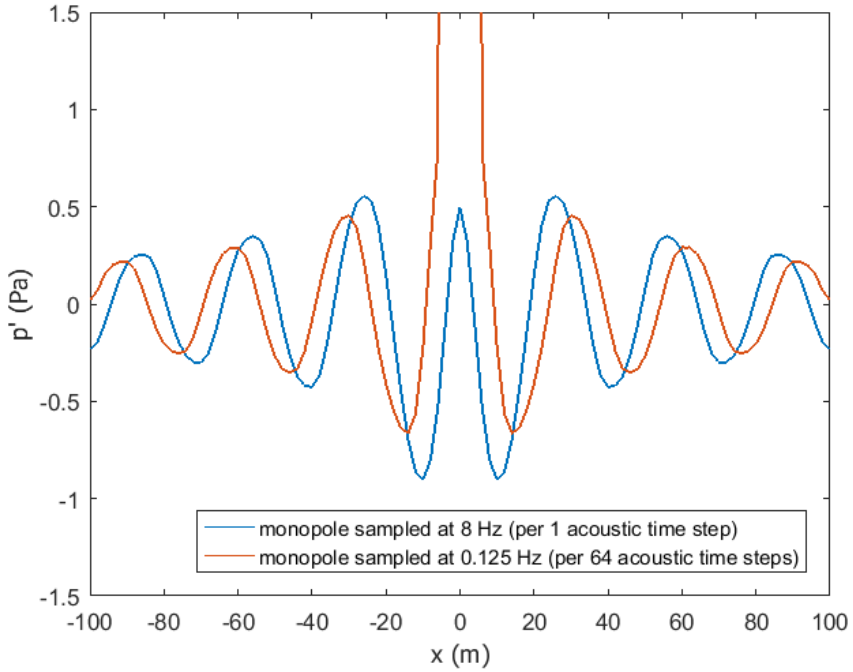

Figure 3.11: Perturbed pressure along centerline at $t = 150s$ (excitation by a monopole).

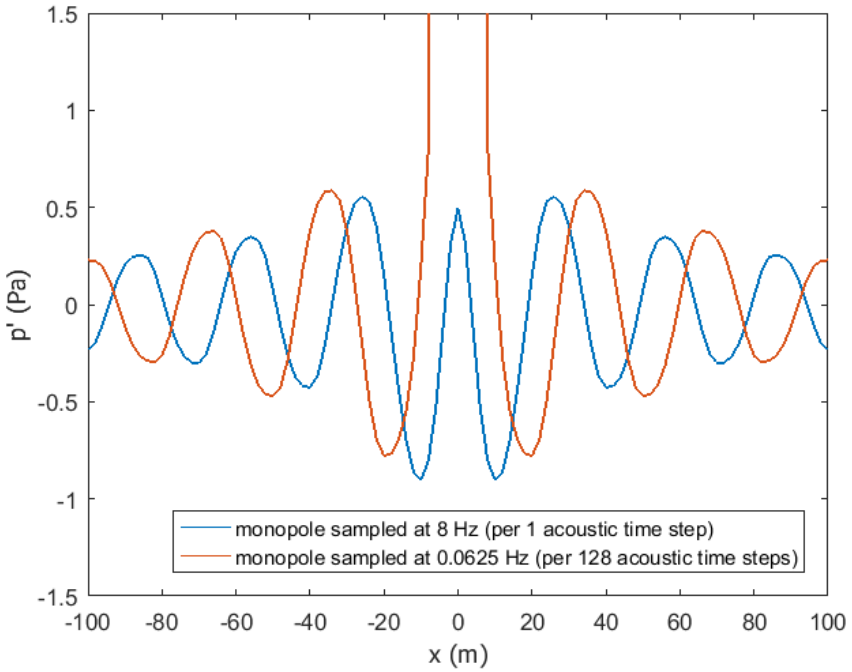

Figure 3.12: Perturbed pressure along centerline at $t = 150s$ (excitation by a monopole).

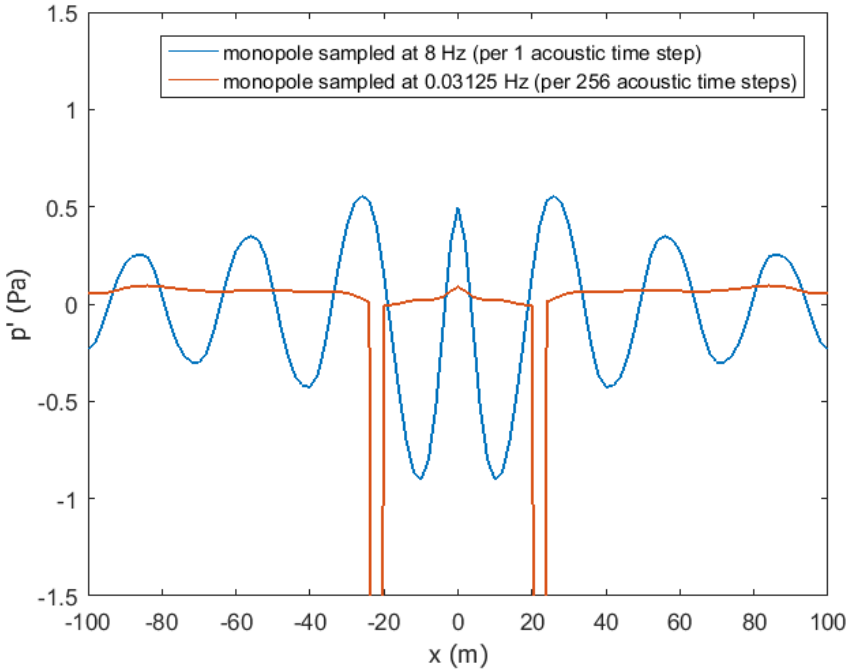

Figure 3.13: Perturbed pressure along centerline at $t = 150s$ (excitation by a monopole).

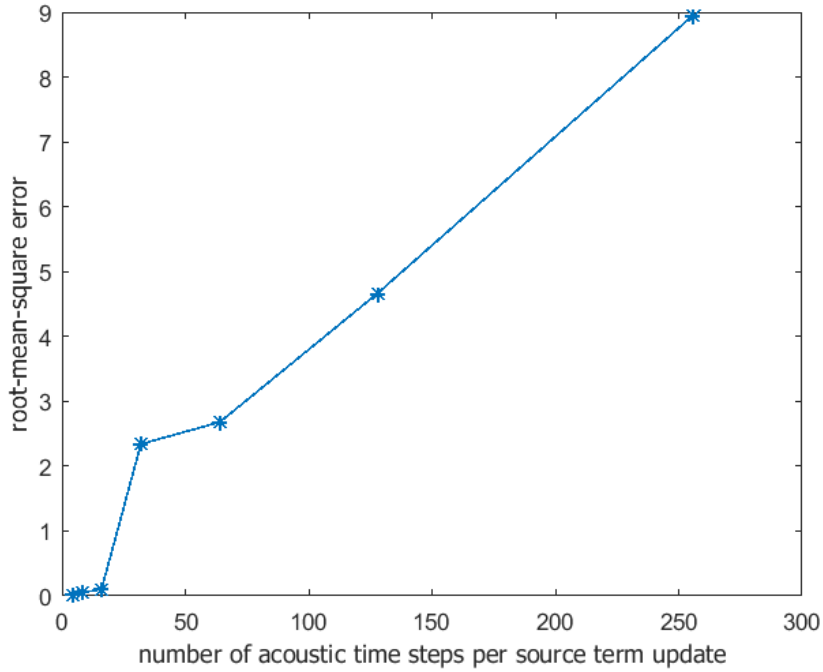

Figure 3.14: root-mean-square error for p' at horizontal centerline of acoustic domain at $t = 150s$ (excitation by a monopole).

From Figure 3.14 it can be noted that the increments of the error are very small for low numbers of time intervals per discrete step. When the value of 16 is reached, which equals a source term update every 2 seconds then the root-mean-square error is sharply increasing.

An analytical source term that is held constant over multiple acoustic time steps is an analogy to a flow solver where the fluid time step is increased in a hybrid aeroacoustic system. It thus results in a lack of source term updates, which causes reduced accuracy in the acoustic results. It can be noted that there is a gradual increase in error, when the discretization exceeds $2s$. This result can be explained by the value of the source term Courant number as is elaborated on in the following paragraph.

In the acoustic solver that is used in this chapter the domain is discretized by a $100X100$ mesh. The domain has dimensions of $200X200$. So the acoustic Courant number equals 0.0625 for a timestep of Δt equal to $0.125s$. Whenever the discretization of the monopole is increased to $2s$, the source term Courant update number is then equal to 1. So supposedly the error gradient thus increases whenever the source term Courant number exceeds 1, which is the case for a discretization larger than $2s$. And from the root-mean-square error graph in Figure 3.15 it can be noted that exactly from value 16 the error is suddenly increasing. An overview of the root-mean-square error as a function of the source term Courant number is given in Figure 3.16.

It can thus be concluded that the ratio between the flow and the acoustic time step number, should not exceed 16 in this solver, because it causes a large decay of the acoustic result. By implementing a new time integration scheme with an interpolation approach the negative effect of a larger time step difference can be decreased. This means that the increase of the root-mean-square error shall be less when the source term Courant number exceeds 1. This enhances the efficiency in the coupling of flow and acoustics.

3.5. Interim conclusion

Based on an analysis of the acoustic results that are produced by a second order accurate (in space) Riemann based LEE solver with a 4-stage explicit Runge Kutta time marching scheme it can be con-

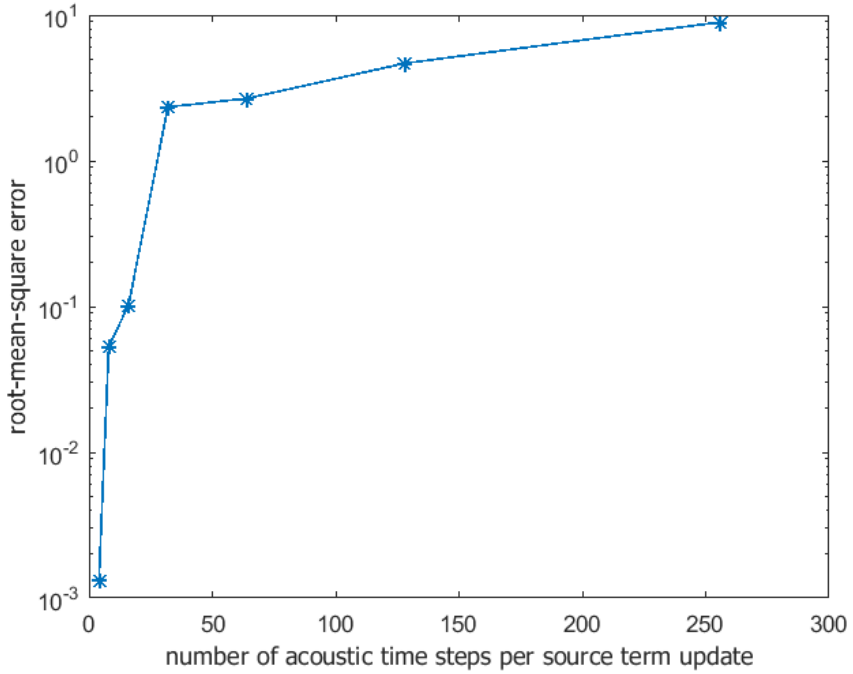

Figure 3.15: semi-logarithmic plot of root-mean-square error for p' at horizontal centerline of acoustic domain at $t = 150s$ (excitation by a monopole).

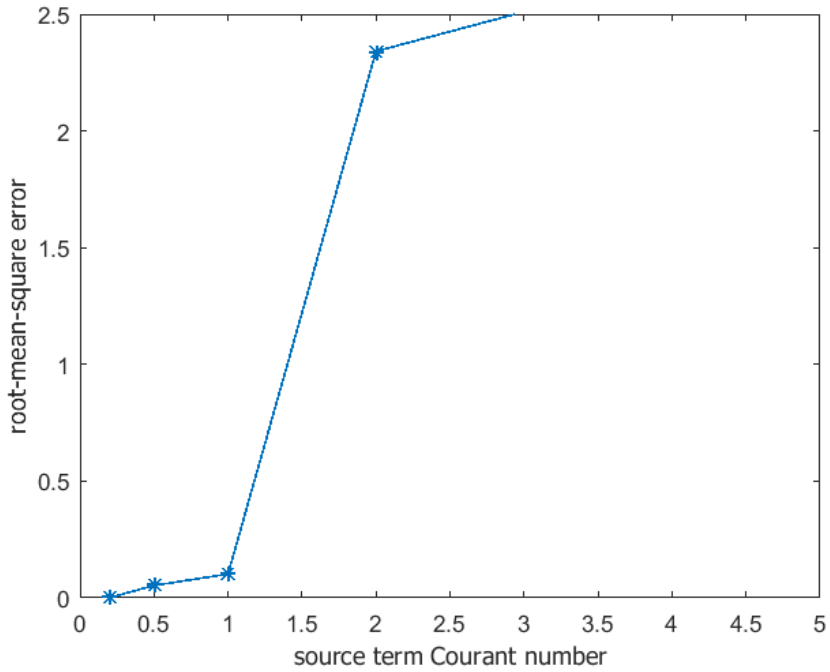

Figure 3.16: root-mean-square error for p' at horizontal centerline of acoustic domain at $t = 150s$ (excitation by a monopole).

cluded that a distortion of the results takes place when the source term Courant number exceeds one. An analytical monopole acted as source term in the acoustic solver. This source term was discretized in time, to simulate the behaviour of an actual flow solver that is feeding source term results into an acoustic solver. When the source term Courant number exceeded the value of 1, it could be noted that a large increase in error occurred. Essentially these results show that when the source term update Courant number is increased then the time step difference between the acoustic and the flow solver cause a significant distortion of the results. It has thus been established that a zeroth order interpolation (which resembles keeping the source term constant for multiple time steps) leads to a distortion of the acoustic results for specific source term Courant numbers. In order to build more efficient hybrid solvers, the source term Courant number at which such a large deviation occurs need to be increased. In this chapter an analytical monopole was used. However when coupling a fluid solver to an acoustics solver, the time step between source updates is the same as the time step used in the fluid solver. When using a higher ratio between fluid and acoustic time step the efficiency can be increased. However by increasing such a ratio an improvement in the transfer to the fluid solver has to be constructed. In order to still attain an accurate solution at the locations that are interpolated, implementation of a higher order time integration methodology is proposed. Therefore the following hypothesis is formulated:

"The maximum time step ratio between flow and acoustic simulations at which a large distortion of the acoustic perturbation results occur can be increased by implementing an improved source term transfer through higher order temporal interpolation and/or higher order time integration of the source term at the node locations"

In the following chapters this hypothesis will be tested. First an accurate interpolation method is determined. Whenever this method is found the time integration at the node locations is explored. Based on a literature study an interesting time integration method has been investigated that uses Gauss Lobatto substepping, which is named the spectral deferred correction method. Due to its nodes locations Lagrange interpolation can be used to interpolate the solution at these locations. This technique will be implemented in the Riemann solver. The analytical monopole test case is used to verify the method. Finally the techniques will be implemented in an LES (large eddy simulation) solver coupled to an acoustics solver, to construct improved source terms.

4

Verification of solution strategy

4.1. Introduction

The right hand side of the linearized Euler equations (LEE) resembles a source term, which is determined by solving the Navier Stokes equations in the fluid as was described in Chapter 2. The temporal source term reconstruction and transfer is investigated in this chapter.

Chapter 3 showed that in order to find an accurate solution the source term Courant number should not exceed one. By using the same spatial grid, the ratio between the required flow time step and acoustic time step is based on the Mach number of the flow as shown by Equation 3.8. Specifically in the case of low Mach numbers a large difference in time step can thus occur for the flow and acoustic equations. A disparity in time scale means that the source term is not updated for every acoustic time step. This leads to a decrease in accuracy of the overall solution. By finding a higher order solution in time in combination with an interpolation of the source term between time levels, the accuracy & efficiency of the acoustic results can be improved.

Multiple solution strategies have been investigated during a literature study. Based on this analysis, the spectral deferred correction method seemed most promising for deriving useful relations. The spectral deferred correction method created by Dutt, Greengard and Rokhlin [15], is an iterative method that uses low order substepping. The correction equation is solved in an iterative manner, increasing the order of the solution for every iteration up to the underlying amount of quadrature nodes. [16]

The spectral deferred correction method unifies two important characteristics: efficient higher order time integration and Gauss Lobatto quadrature. The results at the nodes at which the new time integration method determines the fluid solution need to be interpolated. However using equidistant nodes can prove to be troublesome, in terms of the Runge phenomenon close to the edges of the domain. By applying quadrature nodes in combination with Legendre polynomials this effect can be significantly decreased. Finally, by using Gauss Lobatto nodes the Picard equation can be integrated by means of spectral quadrature, which is exact and thus decreases an important error source. By implementing this method in a hybrid aeroacoustic context, the method can realize a higher order accuracy in time and enable an improved interpolation of the nodes. This then raises the accuracy of the acoustic calculations.

This chapter is roughly divided in four parts. In the first part an analysis is made of the temporal error sources that are existent in a hybrid aeroacoustic solver. In the second part a theoretical background of the interpolation techniques are given. Here both the node spacing and the basis functions are discussed. The source term transfer in the LEE solver is tested by using these basis functions and node spacing to interpolate the discretized monopole source term. The third part of this chapter focuses on the SDC method. Solutions at the node locations are compared to solutions found by the backward Euler (BE) method. The new construction and transfer of the source term are tested by solving the LEE and comparing the result to a solution in which the source term is updated for each acoustic time

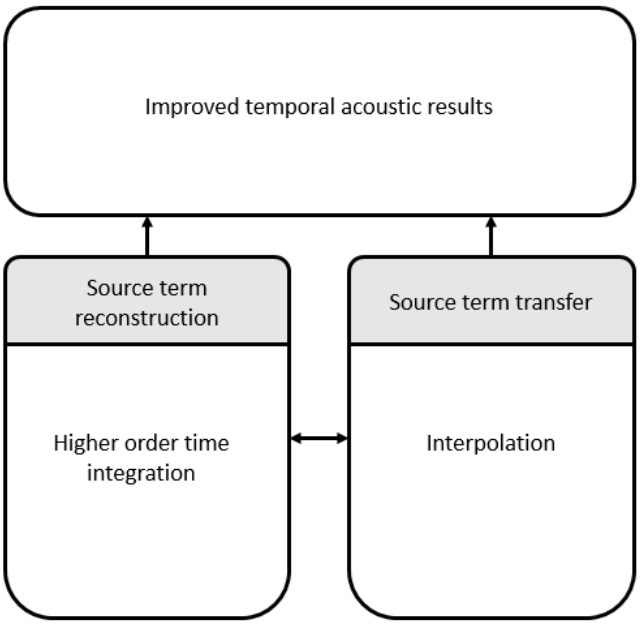

Figure 4.1: Interrelation between higher order time integration and interpolation to obtain improved acoustic results.

step. In the fourth part of this chapter an assessment is made of the relative importance of the time integration method and the interpolation technique.

4.2. Error sources

In Chapter 3 a decay in the acoustic result was observed when the source term was held constant for multiple acoustic time steps. In this chapter the spectral deferred correction method is tested. The source term is transferred to the acoustic solver by interpolation of the solution at the node locations. The acoustic discretization is not altered. This research solely focuses on determining the acoustic accuracy by reconstruction of the source term and the transfer methodology to the acoustic solver.

The temporal error of the acoustic result is governed by the following relation:

$$\epsilon_{acoustic} = \epsilon_{source} + \epsilon_{interpolate} + \epsilon_{\text{acoustic time march}}. \tag{4.1}$$

Here $\epsilon_{acoustic}$, is the total temporal acoustic error. This error is a summation of the source term error at the node locations (ϵ_{source}), the interpolation error ($\epsilon_{interpolate}$) and the error in the time march of the acoustic equations ($\epsilon_{\text{acoustic time march}}$). For all acoustic calculations a $4th$ order Runge Kutta time discretization is used to march in time and an acoustic time step of $0.125s$ was used for every simulation. Therefore the time march error ($\epsilon_{\text{acoustic time march}}$) is held constant. The aim of this research is to decrease the values of ϵ_{source} and $\epsilon_{interpolate}$ in the most efficient way. ϵ_{source} can be decreased by implementation of the spectral deferred correction method and $\epsilon_{interpolate}$ can be decreased through Lagrange interpolation.

The error in the source term construction at the node locations (ϵ_{source}) and the source term transfer ($\epsilon_{interpolate}$) to the acoustic solver are separated. By separating these errors an assessment of the relative contribution to the general acoustic error ($\epsilon_{acoustic}$) can thus be made.

4.3. Source term interpolation

One of the key improvements that can be made in terms of the temporal resolution of the hybrid simulation, is temporal interpolation of the solution at sub steps as shown in Figure 4.2.

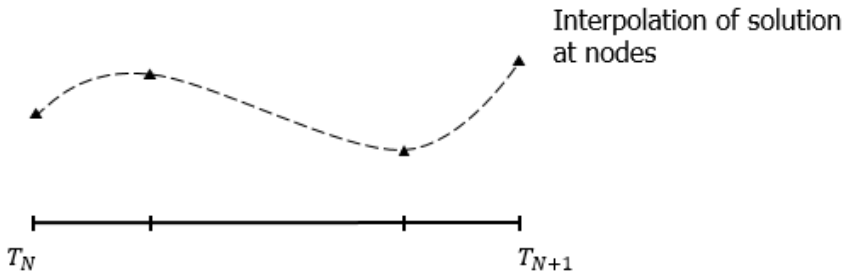

Figure 4.2: Interpolation of the source term solution at the node locations

Implementing such an interpolation in the hybrid solver leads to an update of the source term at each acoustic time step. This is a quasi hybrid solution, since the fluid solution is stored at multiple substeps during a fluid time step. A schematic overview of the quasi hybrid solution is given in Figure 4.3.

During the literature study several basis functions that can be used for the construction of polynomials were studied. Two main basis functions: the monomial basis and the Lagrange basis are tested in this report. Furthermore the node spacing is an essential part of the interpolation strategy. So in this section both the node locations and the interpolation weights are addressed to improve the accuracy of the acoustic result. Normally a non-uniform node spacing can have a negative effect on the function evaluation, however the spectral deferred correction is a higher order method that determines the function values at these non-equidistant nodes. More specifically it uses Gauss Lobatto quadrature, so that the two end-points of the domain are included. In order to test the various node spacings and the construction of the quadrature weights, the discretized monopole from Chapter 3 is used. This monopole was discretized with various ratios to measure the accuracy change of the result compared to the exact solution.

4.3.1. Monomial basis functions

First the monomial basis functions are tested. In order to find a unique solution for a given number of grid points and function values a polynomial interpolation needs to be constructed. Basis functions are used to construct the polynomial. An often used basis is the monomial basis which constructs the following polynomial approximation[17]:

$$\phi(t) = a_0 + a_1 t + a_2 t^2 + \ldots + a_n t^n. \tag{4.2}$$

At the node location the values of ϕ and t are known to construct the polynomial approximation in Equation 4.2. And thus the unknown coefficients need to be determined by solving a system of equations. This is done by setting up a Vandermonde matrix that includes the function evaluations of t:

$$V = \begin{bmatrix} 1 & t_0 & t_0^2 & \cdot\cdot & t_0^n \\ \vdots & \vdots & \vdots & \vdots & \vdots \\ 1 & t_n & t_n^2 & \cdot\cdot & t_n^n \end{bmatrix}. \tag{4.3}$$

By solving the following equation:

$$Va = \phi, \tag{4.4}$$

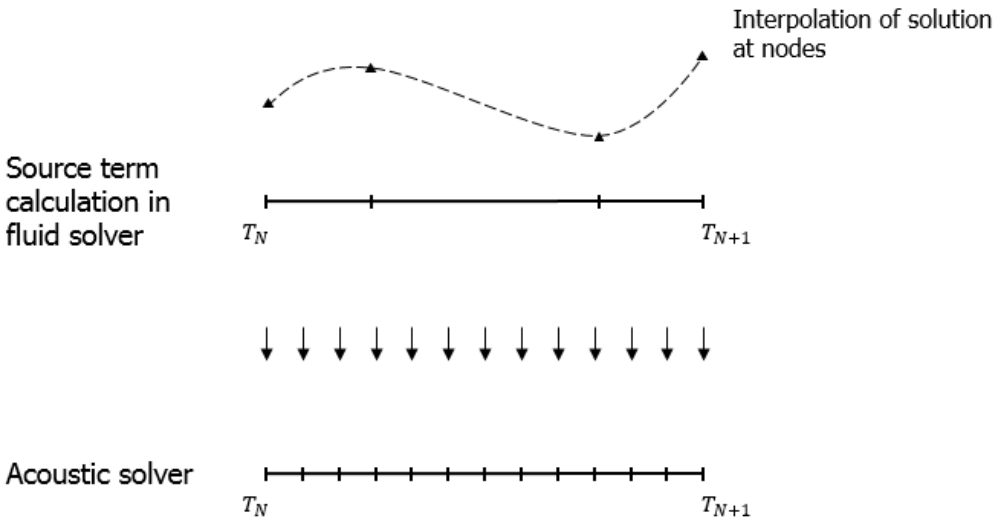

Figure 4.3: Source term transfer from the fluid solver to the acoustic solver

the coefficients a_0 - a_n can be determined. These coefficients then constitute the polynomial function:

$$p(t) = a_0 + a_1 t + a_2 t^2 + \ldots + a_n t^n. \tag{4.5}$$

The above basis functions are used to construct source term interpolations of the known monopole solutions.

4.3.2. Lagrange basis functions

Another interesting technique is the Lagrange polynomial basis. This basis consists of Lagrange multipliers. The Lagrange polynomial approximation is determined by rewriting the systems of equations from Equation 4.4. The Lagrange multipliers are defined as:

$$l_i(t) = \prod_{j=0; j\neq 1}^{j=0} \frac{t - t_j}{t_i - t_j}, i = 0, 1, \ldots\ldots, n \tag{4.6}$$

The value of the polynomial is then determined as:

$$p(t) = f^T l_n(t). \tag{4.7}$$

Here f is the vector containing the function evaluations of the known points and $l_n(t)$ represent the Lagrange multipliers.

The advantage of Lagrange interpolation is that the evaluation of the polynomial approximation does not require the solution of a system of equations as is the case with monomial basis functions. A disadvantage of Lagrange interpolation is that the function does however require the evaluation of the Lagrange multipliers, which can be an elaborate procedure in the case of a large amount of nodes.

So far the theoretical background of interpolation has been discussed. Now the interpolation strategies are applied to the Riemann solver. This is done by improving the source term transfer to the acoustic source term by interpolating the discretized source term updates from Chapter 3. The effect of the

interpolation is quantified by comparing the solution to the case where the harmonic pulsating monopole is updated at every acoustic time step.

4.3.3. Node spacing and quadrature weights

Two basis functions, the Lagrange basis and the monomial basis have been discussed so far. Here the derivation for Gaussian quadrature weights and node locations is discussed.

Concerning the node spacing two approaches are used, i.e. uniform spacing and Gaussian quadrature. Below is described how the Gaussian quadrature weights and locations are determined. This example is shown for three node positions. However this can also be extended to more node locations. The Gaussian quadrature needs to be determined on the domain $[-1, 1]$. Since Gauss Lobatto quadrature is used, the end points of the domain are included in the derivation of the quadrature weights. 3 nodes are used so there are 6 unknowns (weights $c1$, $c2$, $c3$ and locations $x1$, $x2$ and $x3$). To solve for these variables thus requires 6 equations. Six monomial basis functions (defined as g) are required, which are x^0, x^1, x^2 and x^3, x^4 and x^5. Now the equations are determined that guarantee that $2m$ points can be integrated by a polynomial of degree $2m - 1$:

$$\int_{-1}^{1} 1dx = 2 = c_1 + c_2 + c_3 \tag{4.8}$$

$$\int_{-1}^{1} xdx = 0 = c_1x_1 + c_2x_2 + c_3x_3 \tag{4.9}$$

$$\int_{-1}^{1} x^2dx = \frac{2}{3} = c_1{x_1}^2 + c_2{x_2}^2 + c_3{x_3}^2 \tag{4.10}$$

$$\int_{-1}^{1} x^3dx = 0 = c_1{x_1}^3 + c_2{x_2}^3 + c_3{x_3}^4 \tag{4.11}$$

$$\int_{-1}^{1} x^3dx = \frac{2}{5} = c_1{x_1}^4 + c_2{x_2}^4 + c_3{x_3}^4 \tag{4.12}$$

$$\int_{-1}^{1} x^3dx = 0 = c_1{x_1}^5 + c_2{x_2}^5 + c_3{x_3}^5. \tag{4.13}$$

Solving this system of equations gives $c_1 = \frac{1}{3}, c_2 = \frac{4}{3}, c_3 = \frac{1}{3}, x_1 = -1, x_2 = 0$ and $x_3 = 1$. This results in:

$$\int_{-1}^{1} g(x)dx = \frac{1}{3}g(-1) + \frac{4}{3}g(0) + \frac{1}{3}g(1). \tag{4.14}$$

When applying a coordinate transformation from $[a, b]$ to $[-1, 1]$ then $t = \frac{b-a}{2}x + \frac{b+a}{2}$ and $dt = \frac{b-a}{2}dx$. The equation results in:

$$\int_{a}^{b} g(t)dt = \frac{b-a}{2}\int_{-1}^{1} g(\frac{b-a}{2}x + \frac{b+a}{2})dx. \tag{4.15}$$

The above example was used to show how to construct quadrature locations and weights. The equations can be modified for Gaussian nodes by excluding both end points of the domain or Gauss Radau nodes by including only one end-point of the domain. However since the SDC method is using the end-points of the domain, Gauss Lobatto quadrature is used throughout this research.Furthermore different basis functions can be used on the same node locations that thus give different quadrature weights. This will be explained when implementing the SDC method.

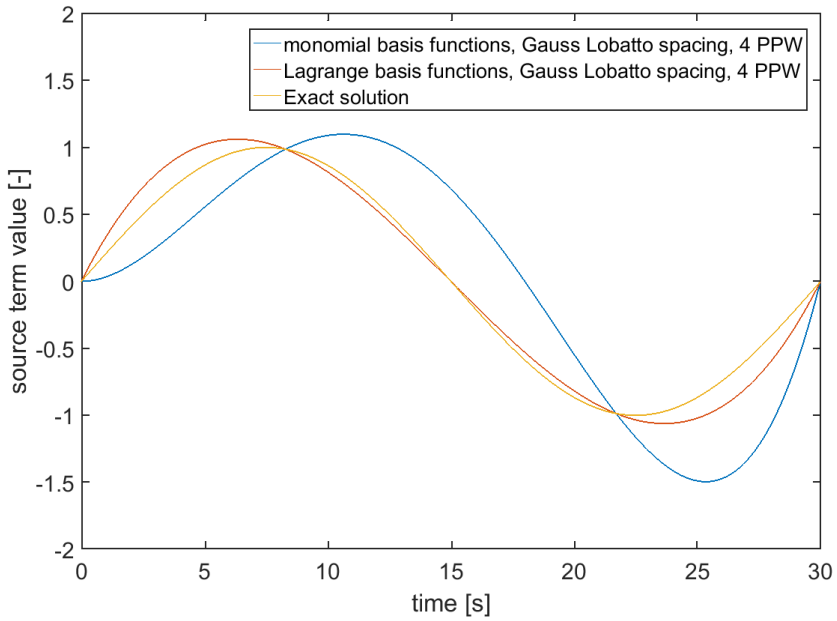

Figure 4.4: Interpolation of 1 period of the analytic source term with monomial and Lagrange basis basis functions using 4 Gauss Lobatto nodes (4 PPW).

4.4. Interpolation verification in monopole excitation

In this section a preliminary analysis is made of the different basis functions and node spacings. To test the effect of interpolation, a source term was reconstructed at 4 PPW (points per wavelength). At first one wave of the source term is reconstructed with the monomial and Lagrange basis function. The results can be viewed in Figure 4.4.

From Figure 4.4 it can be noted that the Lagrange basis functions give a more accurate representation of the source term. The root-mean-square error of the monomial basis function with respect to the exact solution equals 0.4525, whereas the Lagrange basis function gives a root-mean-square error with respect to the exact solution of 0.1099.

In Figure 4.5 an overview is given of the source term representation of monomial and Lagrange basis functions with a uniform node spacing. The Lagrange basis functions still give a more accurate representation of the source term. The monomial basis functions with uniform spacing give a RMS (root mean square) error with respect to the exact solution of 0.4267, whereas the Lagrange basis functions with the uniform spacing give a RMS with respect to the exact solution of 0.1402.

Overall it can thus be noted that the Lagrange basis functions in combination with Gauss Lobatto quadrature give the most accurate representation of the source term.

4.5. Spectral deferred correction method

The spectral deferred correction method is among a relatively new class of iterative methods. The method is characterized by low order iterative sub stepping to minimize the error of the solution. The spectral deferred correction method handles both stiff and non-stiff terms in an ordinary differential equation. In this section an analytic derivation of the method is given, according to [15]. In the spectral deferred correction method the sub stepping within a time step is governed by Gauss Lobatto quadrature. This enables spectral (exact) integration of the integral in the Picard formulation. First the analytic derivation of the iterative method is given for an ordinary differential equation.

Consider the ordinary differential equation,

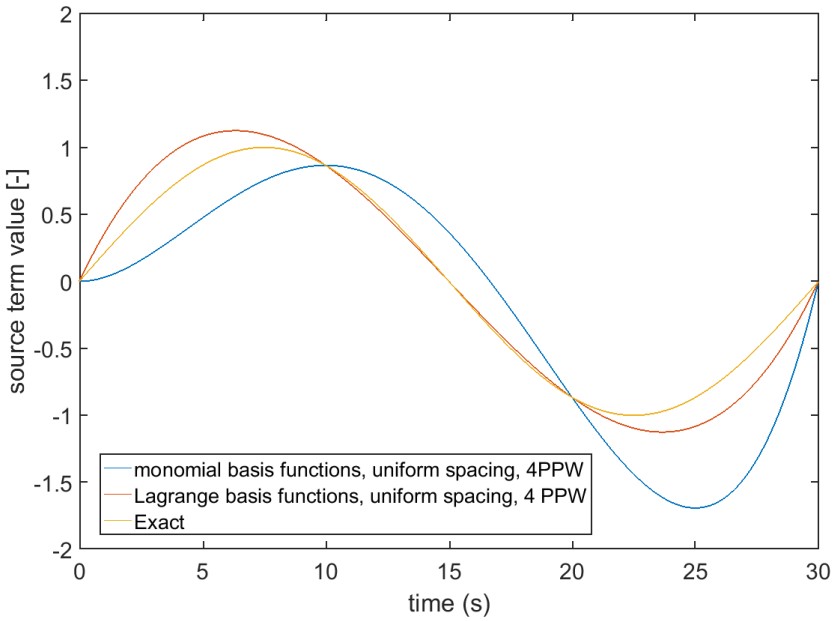

Figure 4.5: Interpolation of 1 period of the analytic source term with monomial and Lagrange basis basis functions using 4 uniform nodes (4 PPW).

$$\frac{d\phi(t)}{dt} = f(\phi(\tau), t), \tag{4.16}$$

with initial value,

$$\phi(0) = \phi_0. \tag{4.17}$$

This Equation can be rewritten in Picard form as:

$$\phi(t) = \phi_0 + \int_0^t f(\phi(\tau), \tau) d\tau. \tag{4.18}$$

Now consider a first approximation, $\tilde{\phi}(t)$ that has been found to this problem by a forward or a backward Euler method. This initial solution contains numerical error $\delta(t)$ and is defined according to:

$$\phi(t) = \tilde{\phi}(t) + \delta(t). \tag{4.19}$$

Here $\phi(t)$ is the exact solution to the problem. Equation 4.18 and 4.19 can be combined to[16]:

$$\tilde{\phi}(t) + \delta(t) = \phi_0 + \int_0^t f(\tilde{\phi}(\tau) + \delta(\tau), \tau) d\tau. \tag{4.20}$$

Furthermore the residual, which is defined as the quality of the approximation, can be defined as:

$$E(t, \tilde{\phi}) = \phi(0) + \int_0^t f(t, \tilde{\phi}(\tau)) d\tau - \tilde{\phi}(t). \tag{4.21}$$

Now rewriting Equation 4.20 and 4.21 results in:

$$\delta(t) = \int_0^t (f(\tilde{\phi} + \delta(\tau), \tau) - f(\tilde{\phi}(\tau), \tau)) d\tau + E(\tilde{\phi}, t). \tag{4.22}$$

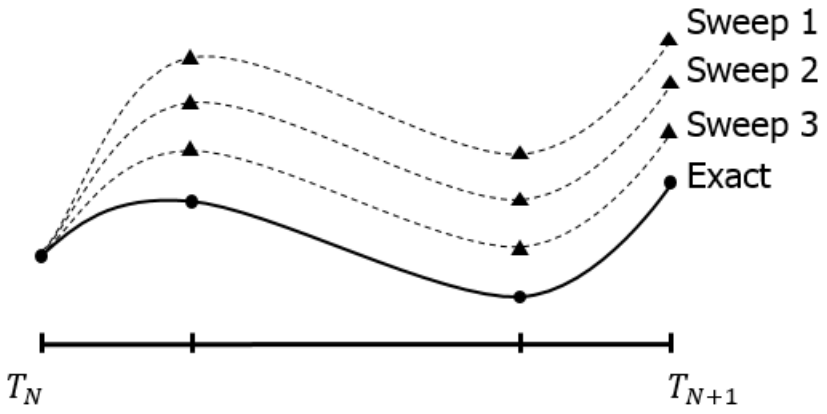

Figure 4.6: In the SDC method the accuracy of the solution at the Gauss Lobatto nodes increases with each sweep till the method converges.

This equation is known as the correction equation [18]. In the SDC method first an initial solution is determined with a low order method. After this, Equation 4.22 can be used to solve for the error. By iterative evaluation of this equation the error is decreased. The accuracy of the approximate solution increases.

So far the analytic derivation of an iterative method has been determined. However it has not been discussed how the integral is determined. Again this determination has been developed in [15].

The Gaussian nodes, $r_1, \ldots\ldots, r_m$ are given on the interval $[a, b]$ by

$$s_i = \frac{b-a}{2} \cdot r_i + \frac{b+a}{2}. \tag{4.23}$$

Consider that these points are associated to a value on their node locations, ϕ, that satisfy a Lagrange polynomial as

$$L^m(\phi, t) = \sum_{i=1}^{m} c_i(t) \cdot \phi_i. \tag{4.24}$$

The functions $c_i(t)$ are based on Lagrange multipliers which are constructed based on the nodal points, according to:

$$c_i(t) = \prod_{j \neq i} \frac{t - t_j}{t_i - t_j}. \tag{4.25}$$

Then if $a = a_0, \ldots\ldots, a_m$ is the result of integrating the polynomial $L^m(f, r)$ as in:

$$a_i = \int_{-1}^{t_i} L^m(\phi, r) dt, \tag{4.26}$$

then the linear mapping is given as:

$$a = S^m(\phi). \tag{4.27}$$

Here the matrix S^m is the integration matrix, containing the quadrature weights. This operator is exact if the polynomial that interpolates the function values at the Gauss Lobatto nodes is of order $m-1$. [15]

4.6. Discretization of the SDC method

The spectral deferred correction method is evaluated by dividing each time step $[T_n, T_{n+1}]$ in a number of Gauss Lobatto nodes. These Gauss Lobatto nodes can be used to find the collocation polynomial over these nodes. [16]

In the SDC method quadrature weights are derived by

$$q_{m,j} = \frac{1}{\Delta t} \int_{T_n}^{t_m} l_j(s) ds. \tag{4.28}$$

The Lagrange polynomial given in Equation 4.28 is constructed, based on the quadrature nodes. When the solution is approximated by a polynomial $u_p(t)$, then Equation 4.28 integrates the polynomial exactly. The following relation can be established as shown in Equation 4.29, where $m = 0, ..., M$.

$$U_m = u_0 + \Delta t \sum_{j=0}^{M} q_{m,j} f(U_j, t_j) \tag{4.29}$$

In order to write the problem more compactly the integration matrix $q_{m,j}$ can be written as a matrix with $M + 1$ rows and $M + 1$ columns, where $q_{m,j}$ denotes all entries of the matrix. Furthermore $\mathbf{U} = [\mathbf{U_0}, ..., \mathbf{U_M}]^\mathbf{T}$ and $F(\mathbf{U}) = [F_0, ..., F_M]^T$.

Equation 4.28 is derived to compute the integral over the entire domain. This integration can be reformulated to find a relation for node to node integration by

$$s_{m,j} = \frac{1}{\Delta t} \int_{t_m}^{t_{m+1}} l_j(s) ds \tag{4.30}$$

Here $m = 1, ..., M$, which can be compactly written by the node to node integration matrix s which contains M rows and $M + 1$ columns.

First the initial conditions are inserted at each collocation node. From here, the SDC iterations start. Equation 4.31 is solved at each node. [16].

$$U_{m+1}^{k+1} = U_m^{k+1} + \Delta t_m [f^E(U_m^{k+1}, t_m) - f^E(U_m^k, t_m)] + \Delta t_m [f^I(U_{m+1}^{k+1}, t_{m+1}) - f^I(U_{m+1}^k, t_{m+1})] + \Delta t S_m^k \tag{4.31}$$

This equation solves the U at every sub step. Here m denotes the substep, whereas k denotes the sweep number. A visualization of the convergence of the solution over each sweep is given in Figure 4.6. Furthermore S_m^k is the vector that contains the integral of the Lagrange multipliers and is used for node to node integration. The equation for S_m^k is defined as

$$S_m^k = s_{m,j} \sum_{j=0}^{M} (F_j). \tag{4.32}$$

Furthermore the above equation is defined both for stiff(f^I) and non-stiff terms (f^E). For the non-stiff terms the forward Euler method is used, whereas for the stiff terms it uses the backward Euler method. The method can also be used with only backward or forward Euler sub stepping.

The order of this method is based on the underlying integration rule, the location of the quadrature nodes, the amount of nodes and the amount of sweeps. For each sweep the order of the scheme increases by one [19]. When the SDC scheme converges it is of order 2M, where M+1 Gauss Lobatto nodes are used [16].

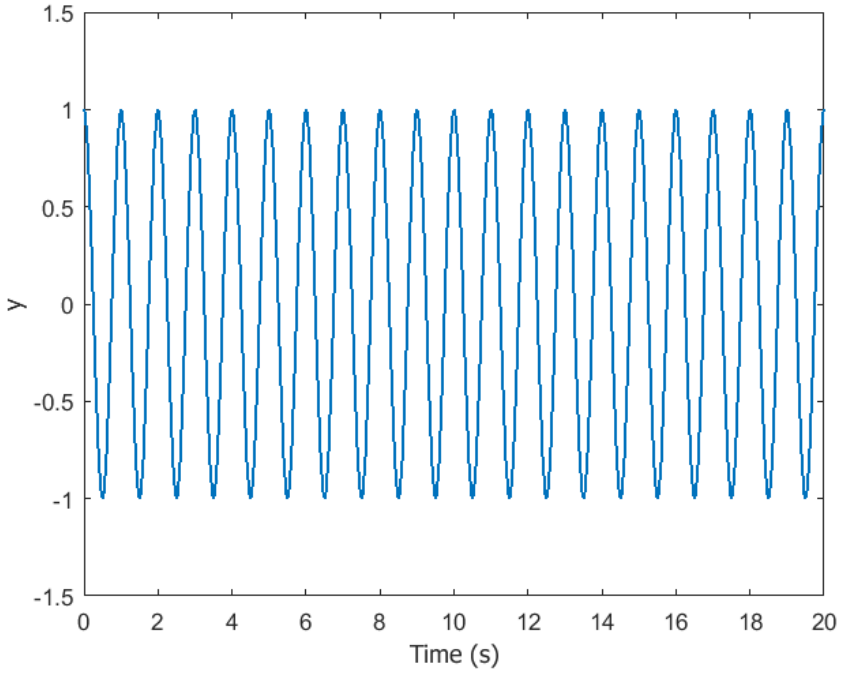

Figure 4.7: Solution by SDC of $y'(t) = -2\pi sin(2\pi t) - 2(y - cos(2\pi t))$, $y(0) = 1$, with 8 quadrature nodes and 9 sweeps.

Convergence of the SDC method can be determined by computing the residual as

$$\mathbf{r}^k = \mathbf{U_0} + \mathbf{QF}(\mathbf{U}^k) - \mathbf{U}^k. \tag{4.33}$$

Here $\mathbf{Q}$ denotes the Kronecker product of the quadrature weights and the identity matrix, which is $\mathbf{q} \otimes \mathbf{I}$. Whenever this residual drops below a pre-defined value then the SDC iteration can be considered converged and one can proceed to the next time step.

4.7. Verification of SDC implementation

The SDC implementation is first applied to the following initial value problem for an ordinary differential equation. The equation is defined as

$$y'(t) = -2\pi sin(2\pi t) - 2(y - cos(2\pi t), \tag{4.34}$$

and has initial condtion

$$y(0) = 1. \tag{4.35}$$

The exact (analytic) solution to this problem is known to be $y(t) = cos(2\pi t)$. The result of the SDC method, which uses 8 quadrature nodes is shown in Figure 4.7 from $t = 0s$ till $t = 20s$. In Figure 4.8 the convergence of the solution with respect to the amount of sweeps is shown.

From this graph it can be noted that the error decreases one order for every sweep.

4.8. Source term reconstruction with SDC

In this final section first the source term is reconstructed by using the SDC method. This way the expected error convergence of SDC simulations can be further verified. This also gives an insight in how the source term error relates to the error in the acoustic result.

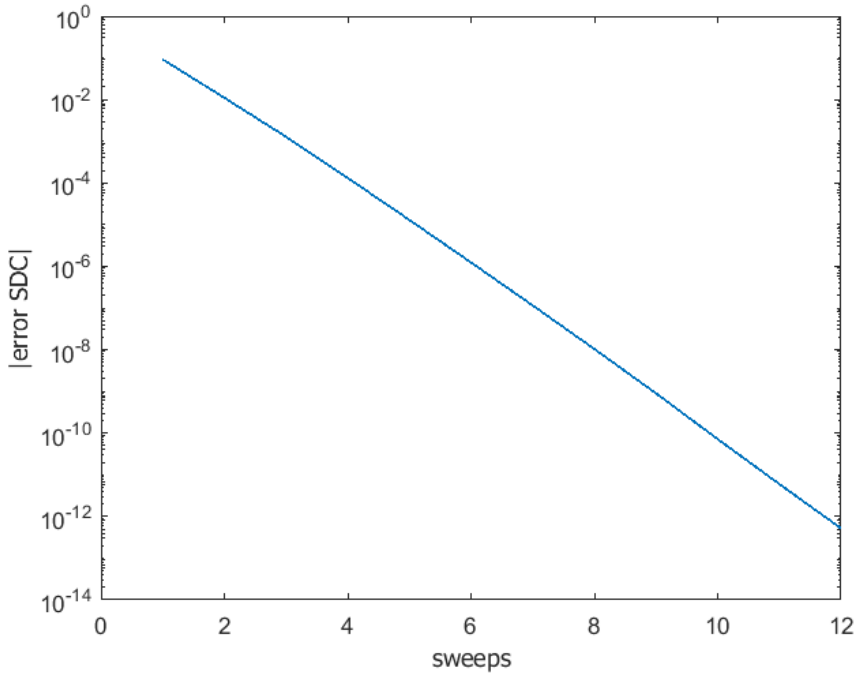

Figure 4.8: Error of the SDC method (8 quadrature nodes) at $t = 20$ with respect to the exact analytical solution.

The source term is reconstructed by solving an ordinary differential equation that has $sin(\omega t)$ as its solution. Both the implementation of the spectral deferred correction method and the backward methodology are compared. The error of both methods is thus measured against the exact solution ($sin(\omega t)$). The underlying function that is being solved, equals $\frac{dy}{dt} = \omega cos(\omega t) - 2(y - sin(\omega t))$. This equation describes an undamped motion that has purely imagery eigenvalues. Therefore the forward Euler method was unstable for step sizes larger than one. This means that the instability of the forward Euler method is not suitable for implementation in the acoustic solver. The backward Euler method is however unconditionally stable, meaning that it can be used in the SDC substepping and as a reference value for the acoustic calculations. In Figure 4.9 it can be noted that the convergence of the backward Euler method is equal to one. The SDC method with 4 nodes is 5th order accurate. The amount of sweeps has been used such that the SDC method converges to the underlying collocation scheme. For the case that 5 nodes are used in the SDC method the order of the solution is equal to 6. When 6 nodes are used the order increases to 7. It can thus be noted that by implementing SDC a higher order method can be constructed.

In Figure 4.10 the error is shown as function of the amount of sweeps. The order of the SDC method converges by one with each sweep. However when dealing with stiff equations, like in this case, the convergence of the method can slow down [16]. Accelerating the convergence of SDC iterations is not part of this research. It can be noted that by increasing the number of nodes in the method the minimum error reduces by an order equal to 1.5.

This section aimed at assessing the correct operation of the higher order methods. It was shown that an equation describing an undamped motion with purely complex eigenvalues could be solved by this method with high accuracy.

4.9. SDC implementation in a hybrid solver

Section 4.7 and 4.3 served as a preliminary assessment of the source term reconstruction and transfer to the acoustic solver. Based on this section it was concluded that monomial basis functions with uniform

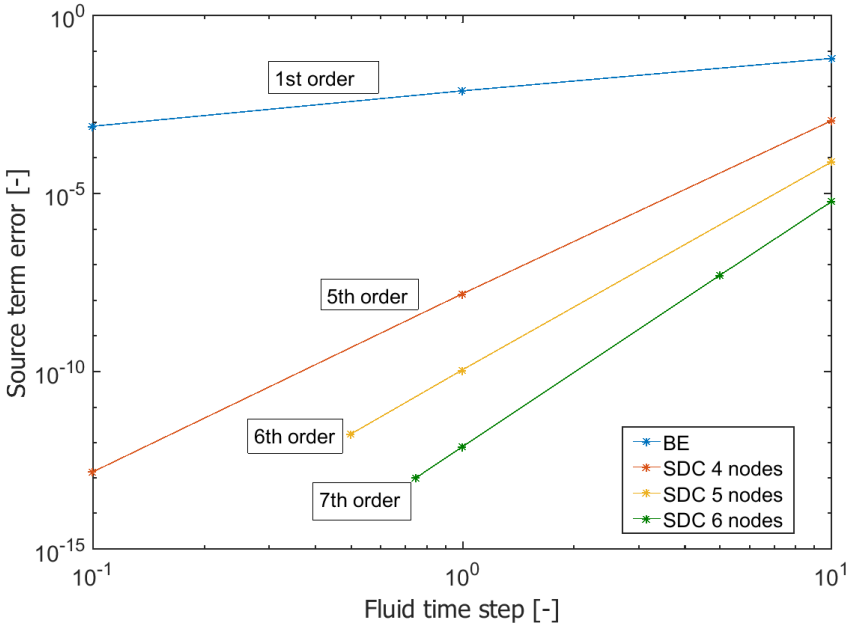

Figure 4.9: Root-mean-square error of the source term solution as function of the time step the the spectral deferred correction method with 4, 5 and 6 nodes and the backward Euler method with 4 nodes.

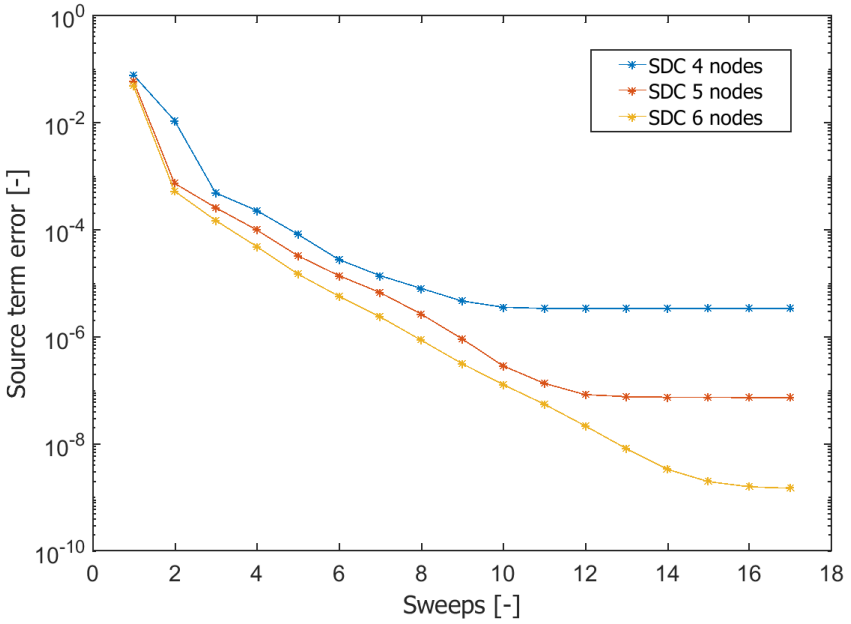

Figure 4.10: Root-mean-square error of the source solution as function of the amount of sweeps.

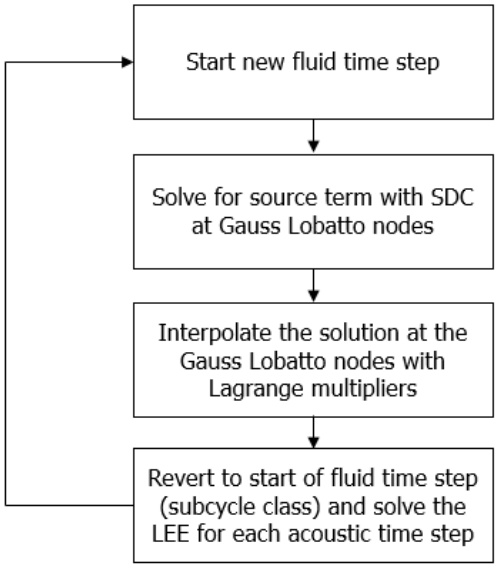

Figure 4.11: Overview of SDC implementation.

nodes were not a feasible alternative for hybrid aeroacoustic implementation. In this section the effect on the acoustics is determined by implementing the SDC method and the Lagrange interpolation in the LEE solver. Furthermore the individual effect of both the Lagrange methodology and the SDC method is investigated.

4.9.1. Test setup

The analytic monopole function is pulsating harmonically along $sin(\omega t)$. In this section an ordinary differential equation that has $sin(\omega t)$ as a solution was defined. The equation that was solved by the SDC method and that thus has exact analytic solution $sin(\omega t)$, is $\frac{dy}{dt} = cos(\omega t) - 2(y - sin(\omega t))$. This equation was solved for each time step in the acoustic solver. Every time step, the dime domain is divided in Gauss Lobatto nodes and the problem is solved over this domain. The result is then interpolated, so that the source terms can be extracted at any point in the time domain.

The periodical time of the sinusoidal monopole is $30s$. So the tests for SDC and interpolation are conducted for smaller time steps than this value. In the SDC method a Courant number of 1, equals a time step of $6s$. The subtsteps of SDC cannot exceed $30s$. Furthermore the tests are run till $t = 150s$, so the total run time has to be a multiple of $t = 150s$. Multiple amounts of SDC nodes were tested for the source term reconstruction, to show the convergence of the method , shown in Figure 4.9 and 4.10. In the hybrid tests the SDC method with 4 nodes is used. This will give a quantitative insight on how a higher order time integration method is improving the acoustic result. In the LEE solver first the source term is solved for the prescribed time step. Then the time step is reverted back (by using OpenFOAM's subcycle class) to the start of the acoustic time steps (with $t_{acoustic} = 0.125s$) to solve the LEE. An overview of the solution algorithm is shown in Figure 4.11. Finally the error is determined by taking the root-mean-square error over the centerline of the domain.

4.9.2. Results

In Figure 4.12 it can be noted that by applying the SDC method in combination with Lagrange interpolation a significant reduction in the root-mean-square error can be found. Again an increase in the root-mean-square error can be perceived when the Courant number exceeds the value of one. How-

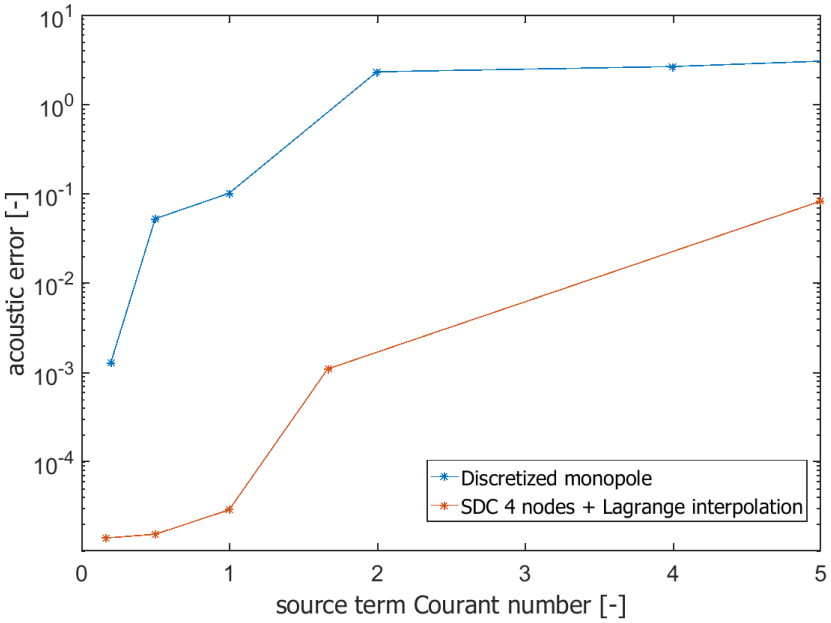

Figure 4.12: Root-mean-square error of the perturbed pressure (at t = 150 s) as function of the Courant number. The blue line shows the result of a discrete samping of the exact monopole, whereas the red line shows the reconstruction of the monopole by using the SDC method and Lagrange interpolation.

ever the acoustic solution still has an error that is multiple orders lower than the discretized (which is zeroth order interpolation) monopole. In this graph the converged solution of the SDC method was used, which means that 10 sweeps were included.

So far a result has been established based on a combination of the SDC method and Lagrange interpolating polynomials. However, as was described in the section about error sources, both interpolation and the time integration method have an individual contribution to the error of the acoustic result. In order to establish the relative improvement of each component a couple of tests are executed that measure the sole contribution of each method.

Figure 4.13 shows the result of the error in the perturbed pressure when only a time integration method is used to resolve the monopole source term. Although the source term can be reconstructed with a significant higher accuracy as was shown in Figure 4.10, the acoustic result does not show such a significant improvement in result.

Since the time integration method analysis did not show the same order of improvement in the acoustic result compared to the improvements that were found by both the higher order time integration and the interpolation, the main contribution to the error reduction comes from the interpolation technique. This is indeed the case when drawing a comparison between the interpolation done by Lagrange multipliers for the uniform nodes and the Lagrange nodes based on the exact solution at the node points. The result can be found in Figure 4.14.

From Figure 4.12, 4.13 and Figure 4.14 it can be noted that the use of Lagrange interpolation has a significant effect on the reduction of the error. It is thus shown that the use of Lagrange interpolation is causing relative to the higher order time integration the largest decline in error. Furthermore from 4.14 it can be noted that the use of Gauss Lobatto nodes is marginally better for a larger disparity in time scales than for a uniform node spacing.

Figure 4.15 shows the difference between a combination of Lagrange interpolation and higher order time integration for both the SDC and BE method with Lagrange interpolation. From this figure it can be shown that the spectral deferred correction method in combination with Lagrange interpolation pro-

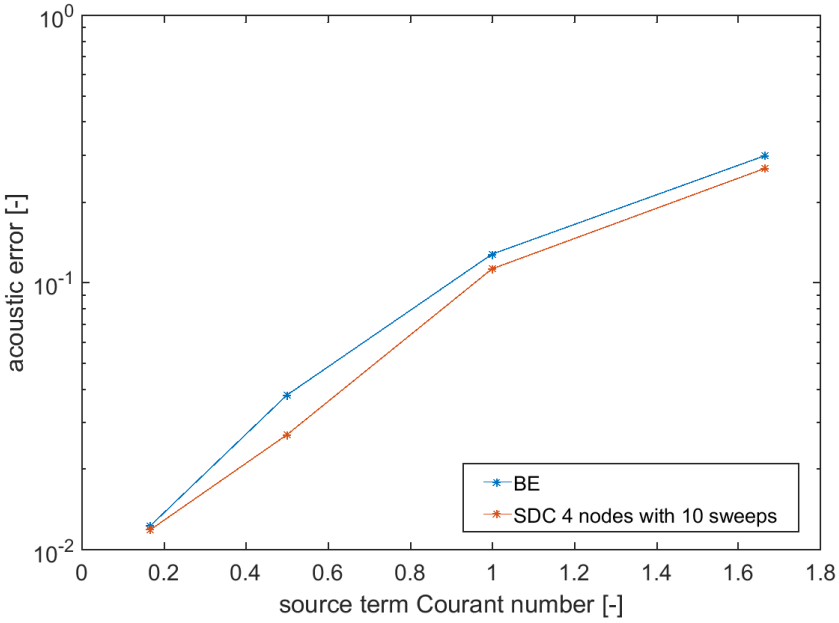

Figure 4.13: Root-mean-square error of the perturbed pressure (at t = 150 s) as function of the Courant number. The blue line shows the acoustic result of the monopole source term constructed with the Backward Euler method and the red line shows the acoustic result of the Monopole constructed with the spectral deferred correction method. Here no interpolation is used.

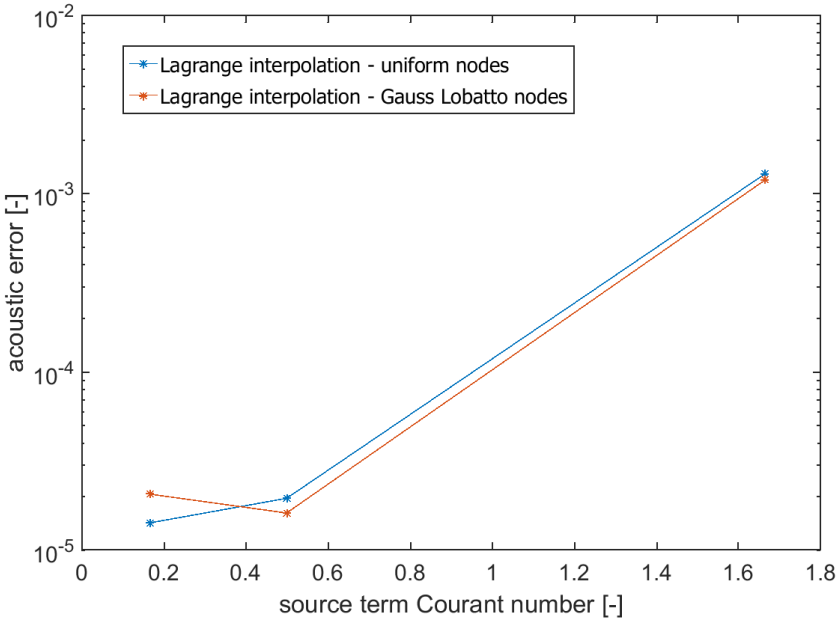

Figure 4.14: Root-mean-square error of the perturbed pressure over the centerline of the domain (at $t = 150s$) as function of the Courant number. The blue line shows the effect of using only interpolation with uniform nodes and the red line resembles the use of Gauss Lobatto nodes. The exact solution of the monopole at the nodes are used.

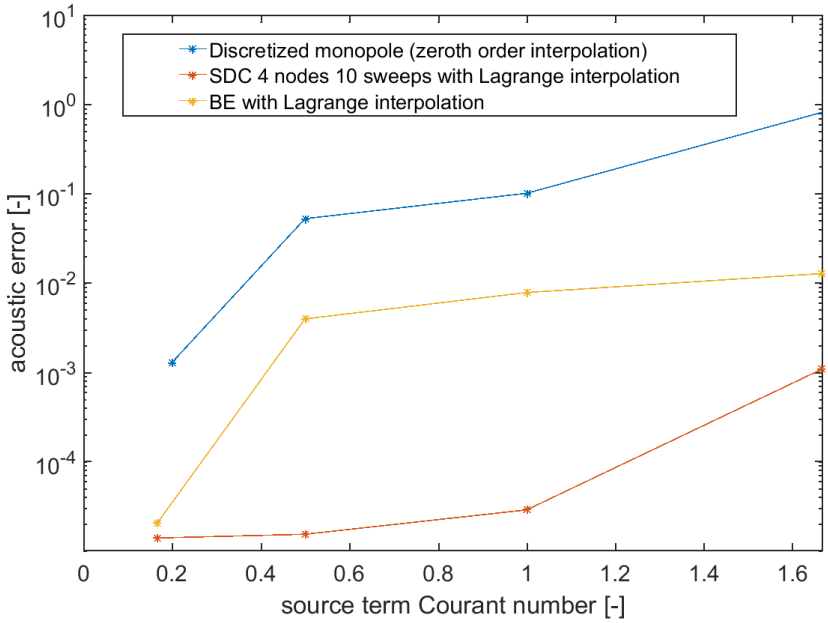

Figure 4.15: Root-mean-square error of the perturbed pressure (over 150 s) as function of the Courant number.

vides the highest accuracy over the range of Courant numbers.

Finally Figures 4.16 and 4.17 show the acoustic error as a function of the source term error. The same acoustic errors from Figure 4.15 are used and the corresponding source term sample time intervals are used to determine the error of the source term. Figure 4.16 shows that already a low acoustic error can be determined for a BE method with a small time step. However when the source term error is increasing, due to an increasing fluid time step, the acoustic error is sharply increasing. Whereas for the SDC method both the source term error and the acoustic error remain low for higher values of the source term error. It can thus be concluded that by the implementation of a higher order source term methodology the acoustic error can be kept lower for more values of the source term error. However when considering the sole effect of the time integration method in Figure 4.17 it can be noted that the overall effect of lower source term error does not have a significant effect on the source term. Based on these results it can be concluded that the acoustic result is mainly dependent on the interpolation of the source term. Thus the main degradation of the acoustic result can then be attributed to the interpolation of the source term at the node locations. Based on Figure 4.16 it can be noted that the lower acoustic error can be attributed to a more efficient Lagrange interpolation by the use of Gauss Lobatto quadrature.

4.10. Interim conclusion

Based on a preliminary analysis of interpolation techniques, Lagrange basis functions in combination with Gauss Lobatto quadrature delivered the highest accuracy. Furthermore the reconstruction of the source term by solving an ordinary differential equation with the spectral deferred correction method showed positive results. The root-mean-square error of the acoustic was decreased compared the BE method .

Based on the reconstruction of the acoustic source term with Lagrange basis functions on a Gauss lobatto grid significant improvements in results are shown. It proves that although using time steps that differ a factor 64 an acceptable mean-square-error could be perceived.

Furthermore the relative effect of the interpolation proved to be highest for reduction of the root mean square error. Also the node spacing showed some difference in accuracy. A SDC implementation with

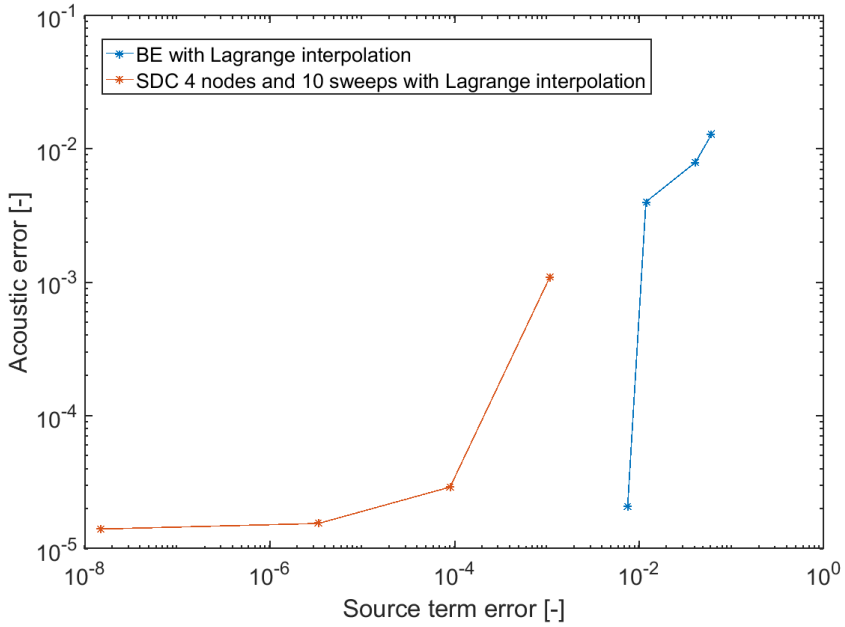

Figure 4.16: The acoustic error as function of the source term error for SDC and BE with Lagrange interpolation.

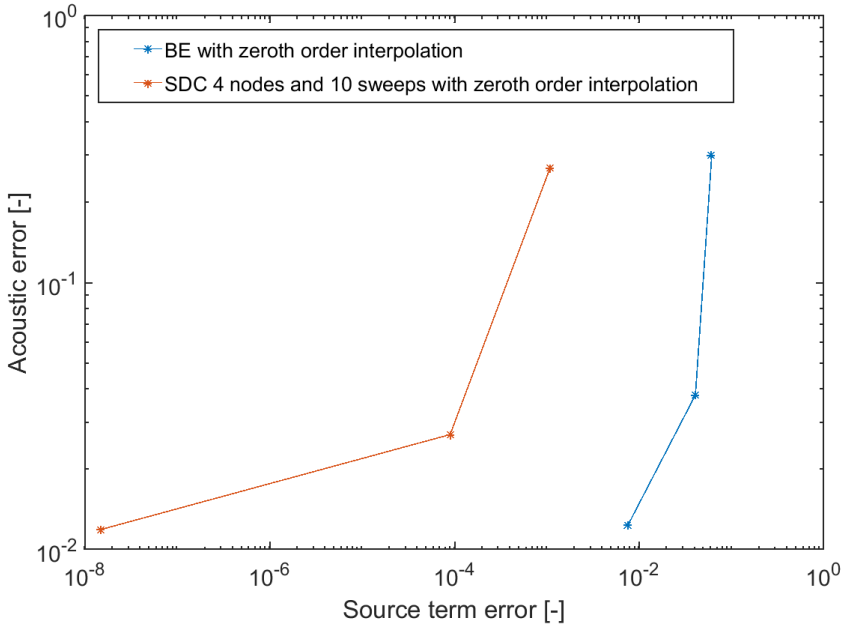

Figure 4.17: The acoustic error as function of the source term error for SDC and BE without Lagrange interpolation.

Lagrange polynomial interpolation gave the highest accuracy. Since the most significant error reduction for this test case was created by interpolation the amount of used sweeps can be decreased to improve the efficiency of the overall implementation.

These tests were based on the reconstruction of a known source term that could be reconstructed by solving an ordinary differential equation. The next step to analyze whether the spectral deferred correction method in combination with Lagrange interpolation improves hybrid acoustics, is to apply the SDC technique in an actual flow solver instead of re-constructing an analytic source term. This comes down to implementation of the SDC solution strategy in a flow solver to solve the conservation equations. Furthermore based on the improved flow results an interpolation can be made to construct an improved source term.

5

Validation of source term reconstruction and transfer in a hybrid aeroacoustic solver

5.1. Introduction

In Chapter 4 the spectral deferred correction method was analysed and tested. An ordinary differential equation, that has the exact solution as source term, was solved. The solution of this equation was then used to solve the acoustic equations in the linearized Euler equation (LEE) solver. The method proved to increase the accuracy when non-matching time steps between flow and acoustics were used. The combination of the spectral deferred correction method and Lagrange interpolation reconstructed the discretized monopole in an efficient way by improving the accuracy significantly.

The next step in this research is to implement the method in an actual flow solver. The source terms can be reconstructed and transferred in a quasi-direct manner to the acoustic solver. The reconstruction is defined as quasi-direct, since the sub steps of the SDC method are stored. Using a quasi-direct approach prevents the need for storing large amounts of data from the flow solver. In this chapter the SDC scheme is implemented in an unsteady, incompressible flow solver. First an investigation is made into the effects of using only Lagrange interpolation based on the solution of the flow at the Gauss Lobatto nodes. No correction sweeps are used in these calculations. Doing a separate analysis of Lagrange interpolation and the SDC corrections before combining both methods will result in a conclusion on the relative effect of higher order time integration and interpolation on the acoustic result.

The test case that is used in this study is the flow through an air-reed instrument[20]. The results from a compressible LES solver and empirical values show that results are in the same order of magnitude. [10] Although the results are in good agreement with the compressible calculations, it is not a target in it self to find a closer resemblance to this result. By implementing the SDC method, the adaptability (scalability) of the flow solver is assessed. An assessment is made whether the implementation of the spectral deferred correction method is able to match the result of a backward Euler method with a small time step.

Acoustic analogies were discussed in Chapter 2. In Chapter 3 a Riemann based solver was used that solved the linearized Euler equations. In this chapter an incompressible, unsteady solver is used to construct source terms to solve Lighthill's acoustic analogy. This analogy assumes propagation in a homogeneous medium. Therefore the acoustic calculations are executed in the far field with respect to the flow region.

First some background information on the reed instrument is given. The validity of the current implementation is shown by comparing the results to a direct aeroacoustic approach and an empirical

relation. Then the pisoFoam algorithm is assessed. The solution algorithm, model geometry, preconditioners, linear solvers and the boundary conditions of the methods are addressed. Then the SDC and Lagrange implementation is shown. Finally the flow and acoustic results from the new implementation are presented and discussed.

5.2. Reed instrument

An air-reed instrument produces sound through the interaction between the oscillation of vortices and the interaction with the edge. Air is blown through the mouth piece and interacts with the resonator. Which is the open cavity of the instrument. At the end of the resonator the air pressure has to be equal to the atmospheric pressure again. In the model a closed cavity is used, which leads to the highest pressure at the end of the cavity. This causes a higher maximum wavelength that can sustain in the cavity and thus a lower frequency.

The edge tones that are caused by the periodical oscillation of the flow and collision with an edge are described through empirical definitions, as derived by Brown [10]

$$\nu = 0.466j(100V - 40)(1/(100l) - 0.007. \tag{5.1}$$

In this formula j is a factor that shows whether a fundamental frequency is determined ($j = 1$) or overtones ($j = 2.3, 3.8, 5.4$). Furthermore V represents the velocity of the flow and l is the distance between the resonator and the edge. The fundamental frequency of the reed instrument can thus be determined. However this value requires a correction, since in the model a closed ended tube is used. The correction is applied by an extension of the length of the instrument. The correction is based on empirical results and in case of the reed instrument equal to $\Delta l = 0.005m$ [10].

First a simulation run is executed for the LES/Lighthill implementation without the SDC method as developed in [20]. In this model the Lighthill equation is solved, using different time steps than in the LES calculations. In order to find sufficient accuracy in the acoustic calculations the subcycle class is used to resolve the dominant frequencies in the acoustic spectrum. The subcycle class in OpenFOAM uses the same length of the time step, but solves the equation over multiple substeps. The N substeps equal Δt in the solution algorithm.

By using sampling points in the solver, the pressure is returned at each point in time. These results are shown by Figure 5.2 in a graph that gives the pressure perturbation as a function of time. In order to compare the results to the direct results from Myamoto [10], a Fourier transform needs to be made. The LES (large eddy simulation) solver uses a discontinuous time step, while the FFT (fast Fourier transform), requires equidistant nodes. The time values are thus interpolated linearly and equidistant values of the pressure are inserted to create the frequency spectrum. In Figure 5.1 results are shown for this implementation.

The fundamental frequency of the reed instrument from Figure 5.1 is $1077Hz$ according to Equation 5.1. Since this value is based on an open reed instrument a correction needs to be applied by extension of the flue. The fundamental frequency that is therefore assumed is $913.1Hz$ [10]. From Figure 5.1 it can be noted that the fundamental frequency is around $1100Hz$. The results from Miyamoto[10], using a direct method, indicate a fundamental frequency of $805.7Hz$. Based on the empirical results and the direct hybrid method, the true fundamental frequency is likely to be lower than the value determined by the hybrid approach. The lower fundamental frequency in the direct approach is also due to the fact that the direct method uses the determined pressure perturbations as feedback to the results. Since this coupling is not existent in a one way hybrid coupling, the fundamental frequency can never be exactly the same. However, due to the fact that the frequency spectrum shows resemblance with a direct solution, it seems as if the solver is finding a correct solution. It thus serves as a good baseline to conduct tests with a new temporal integration approach.

The new implementation aims at improving the determination of the frequency spectrum. At first a simulation is done that uses Gauss Lobatto substepping in the flow solver. The values of the flow field

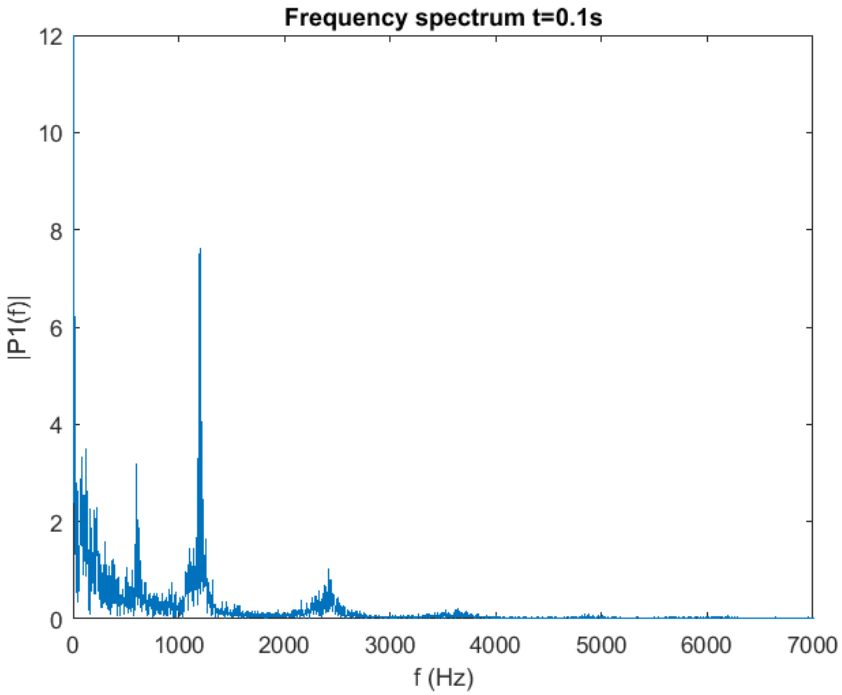

Figure 5.1: Frequency spectrum of LES/Lighthill coupling without SDC and Lagrange interpolation.

that are determined at these locations are interpolated with Lagrange polynomials. By making such an approximation at each flow time step, improved source terms can thus be constructed. The improved source terms are then transferred to the acoustic solver. This solver uses a smaller time step than the flow solver, by using the subcycling class in OpenFOAM.

5.3. Model set-up

In the previous section some background information about the reed instrument was given. The section showed that the model as implemented in OpenFOAM showed sufficient numerical agreement with a compressible (direct) solver. The fundamental frequencies found by Myamoto[10] with a direct compressible solver were lower than for the incompressible solver. This difference can most likely be attributed to the fully coupled aeroacoustic direct method. In this section the model is assessed more precisely.

The flow calculations are done by an incompressible LES (large eddy simulation) solver. The flow results are used to construct source terms that serve as an input to Lighthill's equation. Air is emanating from the mouthpiece with a velocity of $12m/s$. The density perturbations and the pressure are calculated outside the source region. The geometry of the model is shown in Figure 5.3.

5.3.1. Governing equations

Before discussing the PISO algorithm first the governing equations that are solved in the algorithm are treated here. Consider the incompressible Navier Stokes equations, where the continuity equation is defined as

$$\nabla \cdot \mathbf{u} = 0, \tag{5.2}$$

and the momentum equation is

$$\frac{d\mathbf{u}}{dt} + \nabla(\mathbf{u} \cdot \mathbf{u}) - \nabla(\nu \cdot \nabla \mathbf{u}) + \nabla p = 0. \tag{5.3}$$

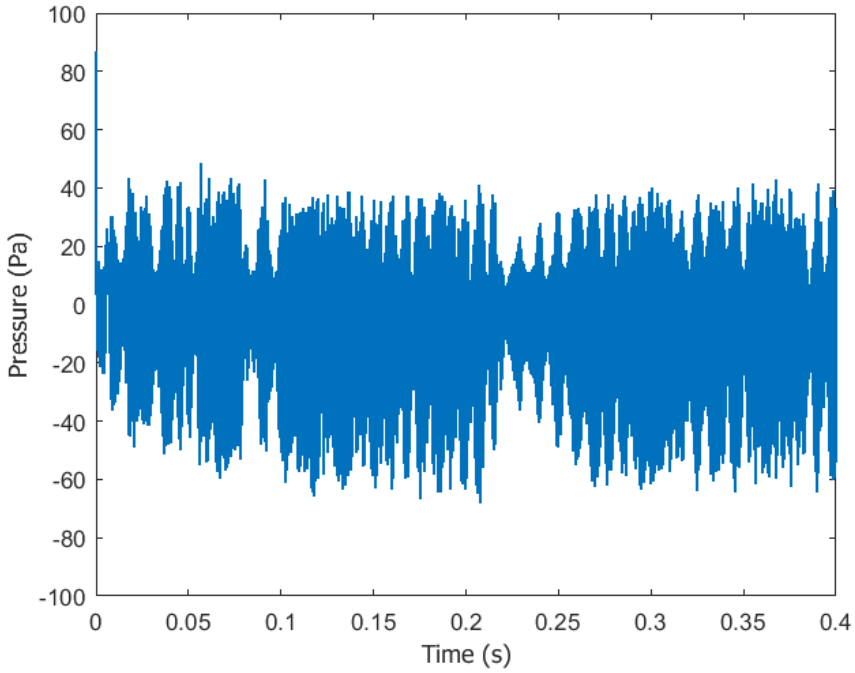

Figure 5.2: Pressure as function of time by the initial implementation (probe located inside the resonator).

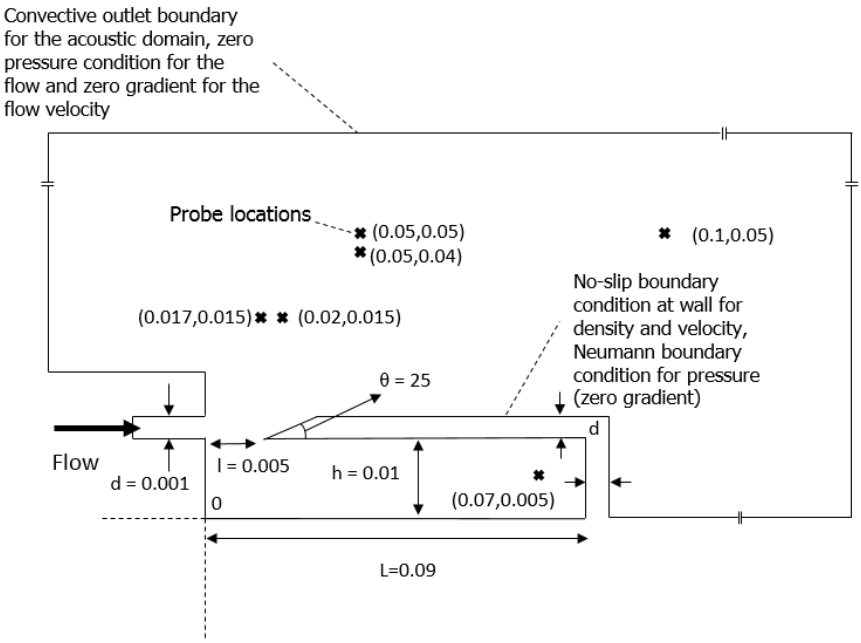

Figure 5.3: Overview of the computational domain around the reed instrument including the probe locations used in this research. Also the boundary conditions are included.

Here $\mathbf{u}$ is the velocity, ν the kinematic viscosity and p the pressure. As is explained in the next section, the PISO algorithm solves the above conservation equations in a segregated manner. At first Equation 5.3 is solved based on the old/initial pressure field. Then the mass fluxes are determined at the faces of the cells. Whenever these values are known, the Laplace equation is solved for the pressure. The Laplace equation is derived by inserting the momentum equation in the continuity equation.

5.3.2. The PISO algorithm

The most well known fluid dynamics applications in OpenFOAM are the PISO (pressure implicit split operator), the SIMPLE (semi-implicit method for pressure linked equation) or PIMPLE (pressure implicit method for pressure linked equation. The last application is a combination of the PISO and SIMPLE applications[21]. In each equation a momentum predictor is solved. Then the pressure equation is solved by adhering to conservation of mass. The value of the pressure is used to explicity correct for the velocity. Both PISO and PIMPLE iteratively solve the pressure equation and correct for the momentum equation. While PIMPLE iterates over the entire system as well. Finally the main differences with respect to the SIMPLE algorithm is that the PISO algorithm uses multiple momentum corrector steps and does not use under-relaxation.

This section describes the operation of the incompressible PISO algorithm which is used for transient flow calculations [22]. The conservations are solved in a 'segregated' manner, meaning that the functions are solved in sequence. In the incompressible calculations there is no coupling between the density and pressure and no coupling to the energy equation. The discretized formulas that are being solved are defined as [22] [23]

$$a_p \mathbf{u}_P = \mathbf{H}(\mathbf{u}) - \sum_f \mathbf{S}(p)_f \tag{5.4}$$

$$\sum_f \mathbf{S}\left[(\frac{1}{a_p})_f (\nabla p)_f\right] = \sum_f \mathbf{S}(\frac{\mathbf{H}(\mathbf{u})}{a_p})_f. \tag{5.5}$$

Here $\mathbf{S}_f$ represents the face surface of each cell, a_p contains the diagonal coefficients of the spatial discretization, $\mathbf{H}(\mathbf{u})$ represents the transport operator that contains the off-diagonal coefficients of the discretization of the momentum equation and a source term (which contains only terms of the spatial discretization in order to maintain temporal consistency [19]), finally p represents the pressure. First the momentum equation as stated in Equation 5.5 is solved for the velocity field using the initial pressure, which is called the momentum predictor. This operation returns an intermediate velocity field. Then the mass flux is computed at the cell faces after which the pressure equation is solved. Multiple non-orthogonal corrections are applied to solve the pressure equation and the mass fluxes at the faces. The non-orthogonality is applied due to the difficulty in unstructured meshes to approximate the gradient of the field at the face [24]. Then the velocities are corrected based on the new pressure field and the boundary conditions are updated. After this the mass fluxes are computed at the cell faces. After the PISO iterations are completed the next time step starts. It should be noted that a colocated grid is used, meaning that all variables are described in the same point. Since in the PISO algorithm a segregated approach is used, the value of the pressure gradient does not depend on the pressure in the adjacent cells. As a result the mass flux does not contain an effect of the pressure, like the a_p coefficients from the momentum discretization. This causes oscillations in the solution [25]. To solve this issue a Rhie & Chow correction is used in OpenFOAM. This expression is not explicitly stated in the PISO algorithm. However due to the Rhie & Chow correction the Laplacian equation for the pressure uses the face values of the pressure based on the neighbouring cells. Finally in these simulations an LES subgrid scale model is used. For some simulations the subgrid model is changed to laminar. This is stated when applicable. A general overview of the PISO algorithm is shown in Figure 5.4.

5.3.3. Geometry

The geometry of the model can be observed in Figure 5.3. Probe measurements are done at various locations in the domain. As Lighthill's acoustic analogy is not applicable inside the flow domain, probe

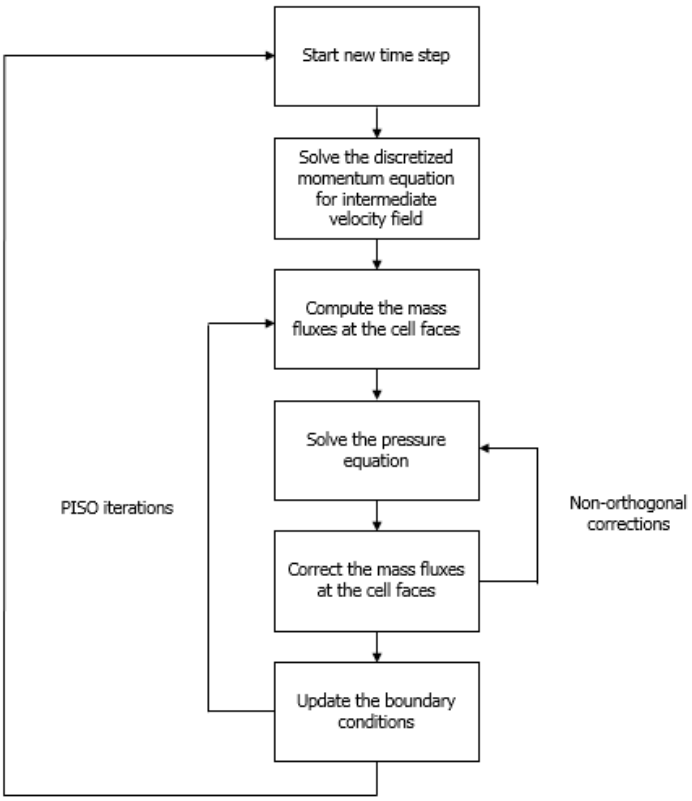

Figure 5.4: Overview PISO algorithm.

locations are required outside the active flow (source) region. In Figure 5.5 the solution of the perturbed density can be perceived at $t = 0.18s$. Furthermore the axis shows the dimensions to which can be referred when data is plotted over time in this chapter.

5.3.4. Solvers

So far a broad outline was given of the PISO algorithm, which contains all the equations that are being solved. However within this group of equations, like the pressure equation, the momentum equation and the continuity equation, require individual linear solvers, that solve the matrix equations in an iterative manner. In this section the used solvers are elaborated on, and it is shown which underlying equations are solved. Furthermore the pre-conditioners, which are used to ensure faster convergence of the solution of matrix equations are being described. When running the code, the number of iterations and the residuals by the solvers are shown. The residual is calculated by inserting the new found solution in the equation. The left and right hand side of the equations are then used to quantify the convergence of the solution. No under-relaxation is applied in the simulations. For the pressure equations the DILU (Simplified diagonal-based incomplete LU pre-conditioner) was used, which uses lower (L) triangular and upper (U) triangular matrices to accelerate solving matrix equations for assymetric matrices. The lower triangular matrices are not sparse and therefore demand memory requirements. For the symmetric matrices the DIC pre-conditioner is used, which is the symmetric version of DILU. The Laplacian terms and the time derivative terms use the DIC pre-conditioner, whereas the convective terms and the turbulent terms use the DILU pre-conditioner. In terms of linear solvers the matrix equations with symmetric matrices are solved with the PCG (preconditioned conjugate gradient) solver. While for the asymmetric matrices the PBiCG (Preconditioned bi-conjugate gradient) solver is used [26].

5.3.5. Boundary conditions

The inflow uses a uniform horizontal velocity of $12m/s$. The pressure at the inlet is defined by a Neumann boundary condition. At the outlet the boundary is set to zero for the pressure and a Neumann

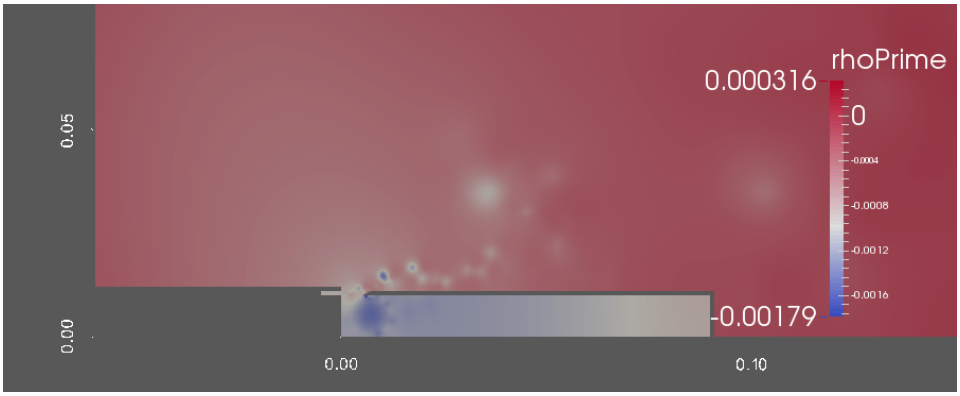

Figure 5.5: Reed instrument immersed in flow at $t = 0.179846s$, density perturbation (ρ') in the acoustic domain is shown. The dimensions are shown on the x- and y- axis.

boundary condition is used for the velocity. Furthermore for the acoustic calculations the boundary conditions are defined by the convective outlet boundary determination, which is the same condition as used for the LEE solver in Chapter 3 and Chapter 4. For the flow simulation Neumann boundary conditions are used for the pressure and a no-slip condition is used for the velocity and density at the walls [20].

5.4. Implementation of SDC

The SDC method is implemented by building outer corrections in the pisoFoam algorithm over the PISO iterations. In order to start the simulation a backward Euler time step is calculated over the sub steps. The sub steps are defined by dividing the fluid time step in a number of Gauss Lobatto nodes. The next step again a backward Euler is used to find all function evaluations at the nodes. Then the first sweep is initiated in which the SDC correction equation is solved implicitly for every sub step. Finally the result at the Gauss Lobatto nodes are interpolated through Lagrange multipliers. It should thus be noted that due to the left end point requirement that the function evaluation is required at the first node. Since this value can not be determined when starting the simulation the first step is computed by using a backward Euler method.

The implementation of the spectral deferred correction method, means that a source term is included in the right hand side of the discretized momentum equation. In this research the incompressible Navier Stokes equations are solved, which are defined as,

$$\nabla \cdot \mathbf{u} = 0 \tag{5.6}$$

$$\frac{d\mathbf{u}}{dt} + \nabla(\mathbf{u} \cdot \mathbf{u}) - \nabla(\nu \cdot \nabla \mathbf{u}) + \nabla p = 0 \tag{5.7}$$

Whenever these equations are discretized by the finite volume approach and operators are determined for solving these equations, the following equation remains[19]:

$$\frac{d\mathbf{u}}{dt} = H(\mathbf{u}) - a\mathbf{u} - \nabla p. \tag{5.8}$$

In this formulation $H(\mathbf{u})$ is the spatial discretization, consisting of a source term $\mathbf{q}$ and $-B\mathbf{u}$, which are the off diagonal coefficients multiplied by the fluid velocity. In order to set up an initial value problem with improved time integration the source term $H(\mathbf{u})$ can only include the spatial discretization contributions[19]. Then if this is the case the following ordinary differential equation remains:

$$\frac{d\mathbf{u}}{dt} = F(\mathbf{u}, p, t). \tag{5.9}$$

As was stated in this chapter, Equation 5.9 is solved by applying the backward Euler method. However in this research a new time integration method, the spectral deferred correction method, is implemented. This method has a different right hand side as was shown in chapter 4. First the discretization of the backward Euler is defined as

$$\frac{\mathbf{u}_{m+1} - \mathbf{u}_m}{t_m} = F(\mathbf{u}_{m+1}, p_{m+1}, t_{m+1}). \tag{5.10}$$

Here m denotes the Gauss Lobatto substepping. In the following equation the spectral deferred correction method is applied to the initial value problem in Equation 5.9. This results in a different formulation, as shown in Equation 5.11. The analytic derivation of the method was shown in Chapter 4. Here S_m^k is the node to node integration by multiplying the integration weights with the function values on the nodes. The SDC formulation is defined as

$$\frac{\mathbf{u}_{m+1} - \mathbf{u}_m}{t_m} = F^{k+1}(\mathbf{u}_{m+1}, p_{m+1}, t_{m+1}) - F^k(\mathbf{u}_{m+1}, p_{m+1}, t_{m+1}) + S_m^k. \tag{5.11}$$

It can thus be noted that Equation 5.11 contains a more elaborate right hand side than the backward Euler method in Equation 5.10. The extension of the right hand side means that the momentum predictor gets an extra source term on the right hand side, which is a summation of the function evaluation at the previous iteration and the node to node integration term. This term is defined by spectral quadrature.

5.5. Implementation of interpolation approach

As the new higher order time scheme is implemented a more accurate representation of the velocity at the nodes should be perceived. However another important aspect of the source term reconstruction is the interpolating polynomial. Due to the fact that 3 substeps are used in the determination of the velocity field, these values are stored at the nodes. Due to the fact that the nodes are created by Gauss Lobatto quadrature an accurate approximation of the polynomial over the domain can be made.

The Lagrange script is built by decomposing the velocity vectors, so that the Lagrange script can be solved based on scalars. The Lagrange approximation is determined by determining the Lagrange multipliers with

$$l_j(x) = \prod_{0 \leq m \leq k} \frac{x - x_m}{x_j - x_m} \tag{5.12}$$

and multiplying these with the known values at the nodes. In the PISO algorithm the subcycling class is not only implemented in the acoustic solver, but also in the flow solver. The time step is subdivided in the Gauss Lobatto substeps. During a timestep, the substep velocity data is saved. This data is then used as input to the Lagrange script. To do so, additional volume vector fields are loaded in OpenFOAM. Furthermore the solver is using a constant time step. Due to Lagrange sub stepping the time step is smaller, so that the flow Courant number decreases in the new implementation. A visual overview of the modified algorithm can be found in Figure 5.6.

5.6. Flow results

In this section the flow results are discussed after implementing the spectral deferred correction scheme. In this section the flow solver is disconnected from the acoustic solver. This way it is possible to efficiently check the implementation of the spectral deferred correction method. In the previous chapter the spectral deferred correction method was used to solve ordinary differential equations. In this implementation as discussed in the previous section, the SDC method is implemented around the PISO algorithm to improve the accuracy and efficiency of the flow solution.

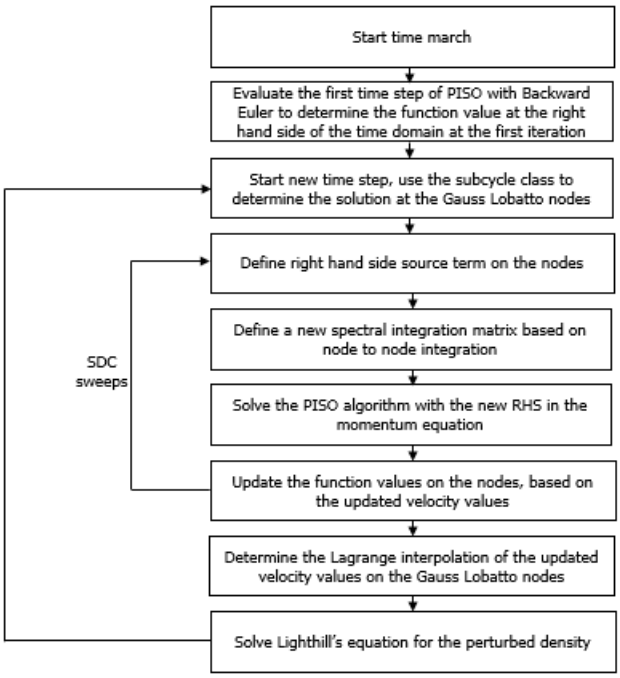

Figure 5.6: Hybrid solver that incorporates the SDC methodology.

A large pressure difference occurs at the start of the simulation. This pressure peak is due to initial conditions which accelerate the flow from zero velocity in the nozzle, instantly to $12m/s$. This causes a (theoretical) infinite acceleration. In general a smaller time step leads to an improved accuracy. However, due to the way that the initial conditions are introduced, a small time step can lead to very high accelerations and cause a divergence of the simulation. By using a variable time stepping condition, the initial part of the simulation is stabilized. Although the simulation has an unsteady nature, such pressure spikes do not occur for the rest of the simulation. However for the sake of testing the acoustic accuracy it is important to use a constant time step, as the Gauss Lobatto nodes are predetermined with respect to each other. Using a variable time step, would not work in combination with a higher order time approach that uses Lobatto quadrature. Therefore the simulation is saved at $0.17s$ and used as initial condition for the tests. This avoids having to cope with the large pressure peak at the start of the simulation.

In Figure 5.7 the convergence of the error is shown for the BE and SDC method. The error is determined with respect to a reference solution that is computed with a BE stepsize of $t = 1e-7s$. Furthermore a laminar subgrid scale model is selected with a kinematic viscosity of $1.46 \cdot 10^{-3} m^2 s^{-1}$. It can be noted that the SDC method, that uses 3 sweeps produces a lower root-mean-square error for a time step of $1e-5s$. However the error for $t = 1e-6s$ is the same as for BE. The error convergence that was shown in Figure 4.9 cannot be perceived in this implementation.

5.7. Acoustic results

Finally the acoustic results are determined when the solver uses a turbulent model and a lower kinematic viscosity, which is $1.46 \cdot 10^{-5} m^2 s^{-1}$. This is a more realistic setting for noise prediction. In these tests different fluid time steps are used. Here the BE solution is determined over the Gauss Lobatto nodes. For one simulation run, the solution at the nodes is interpolated by Lagrange multipliers. For the reference solution a fluid time step of $dt = 1e-7s$ was used and 2 acoustic subcycles. For the other two test cases a fluid time step of $1e-5s$ was used and 200 subcycles. Different acoustic subcycles between the reference solution and the test cases are used to have the same acoustic time step, which is $5e-8s$. This way the discretization error of the acoustic simulations, as described in section 4.2,

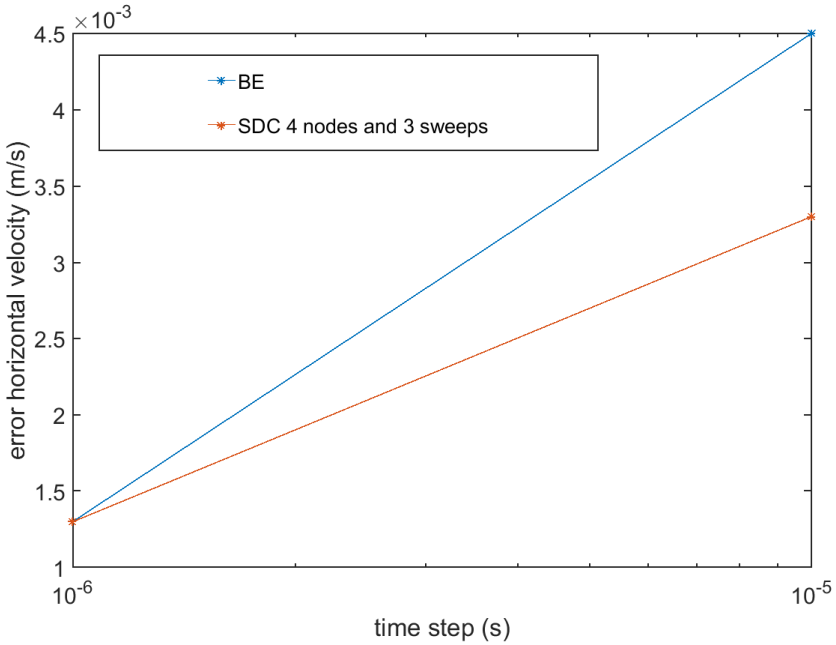

Figure 5.7: Root-mean-square error of the horizontal velocity field over the entire grid.

is held constant. The results are shown for different probe locations in Figure 5.8-5.10. For a visual representation of the probe locations given below each graph, one can refer to Figure 5.5.

Figure 5.8 shows a probe location in the region where the fluid behaviour is active. At $t = 0.002s$ a clear difference between zeroth order interpolation and Lagrange interpolation can be perceived.The RMS (root-mean-square) is reduced with 11 percent. Figure 5.9 shows the acoustic result at a slightly different probe location. The Lagrange interpolation at the Gauss Lobatto nodes, shows a close resemblance with the reference solution. Whereas the BE method which uses zeroth interpolation (which is a constant source term between substeps), shows some deviations of the reference solution. The RMS is reduced with 7 percent by using Lagrange interpolation. Finally the acoustic results in the far field, away from the active source region, are shown in Figure 5.10. Here, hardly any difference can be perceived between the reference solution and the results with and without interpolation at the quadrature nodes.

5.8. Interim conclusion

In this section a hybrid aeroacoustic solver was used that constructs source terms with an incompressible LES solver. The PISO algorithm is modified to accommodate Gauss Lobatto substepping. At the node locations the velocity fields are stored. The velocity fields at the node locations were interpolated by a Lagrange polynomial to construct improved source terms for solving Lighthill's equation. Furthermore the SDC method was implemented around the PISO algorithm. Based on the results, it can be concluded that the SDC method did not show the same error convergence as was determined in Chapter 4. The SDC method decreased the root-mean-square error over the entire domain at a time step of $dt = 1e-5s$ compared to the BE method. However for a time step of $dt = 1e-6s$ the root-mean-square error was identical to the BE method. Finally the interpolation error was assessed. Implementing Lagrange interpolation at the node locations improved the acoustic result in the active source region. In the far field acoustic results were similar for both zeroth order interpolation and Lagrange interpolation.

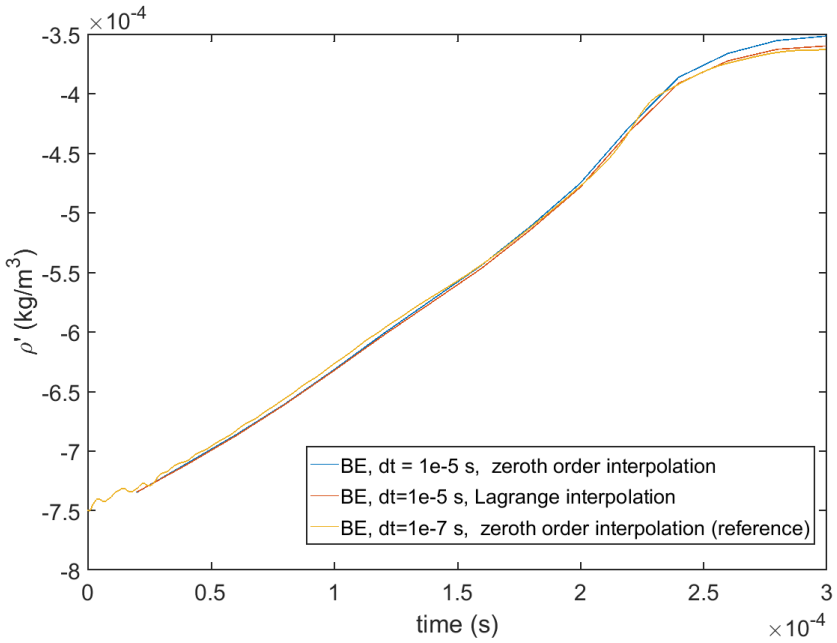

Figure 5.8: Density perturbation (ρ') at probe location (0.017;0.015) as a function of time (s), 50 acoustic sub cycles were used for each simulation.

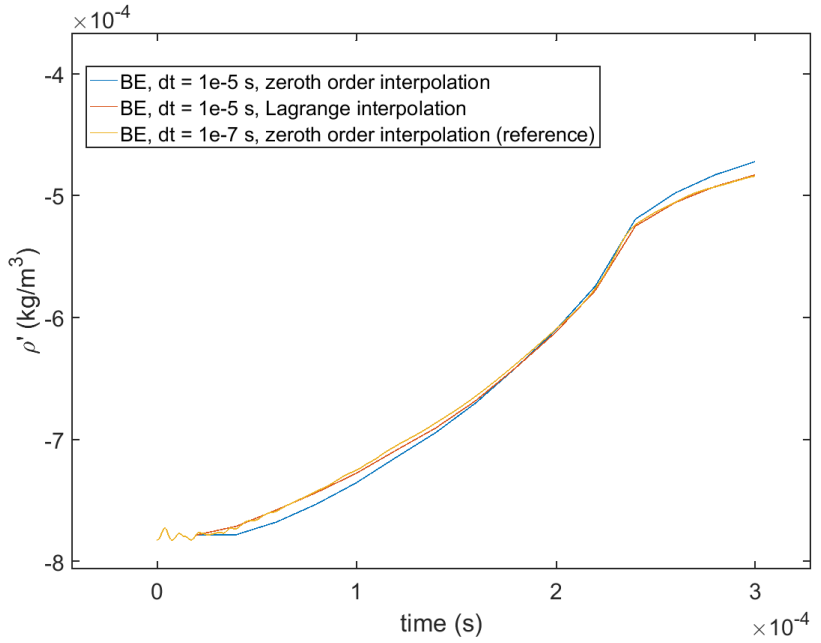

Figure 5.9: Density perturbation (ρ') at probe location (0.02;0.015) as a function of time (s), 50 acoustic sub cycles were used for each simulation.

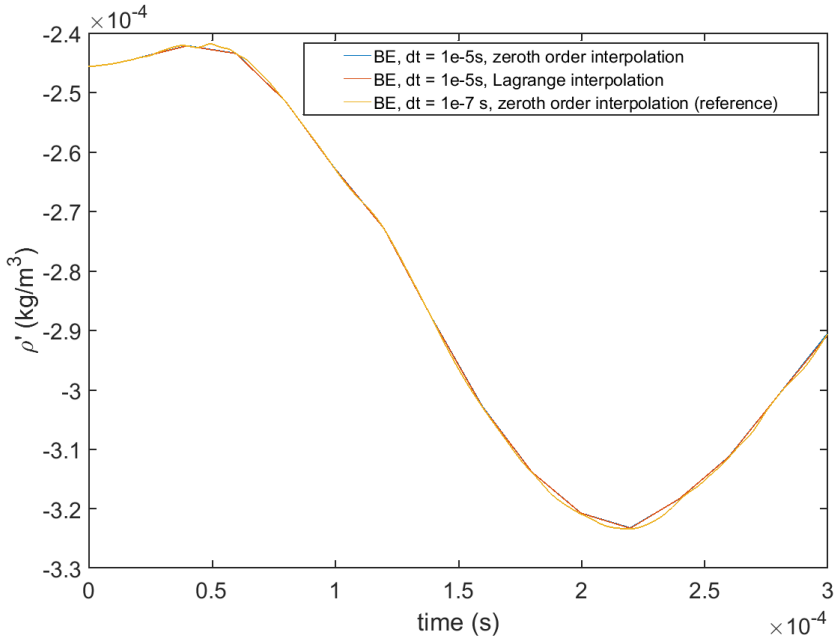

Figure 5.10: Density perturbation (ρ') at probe location (0.1;0.05) as a function of time (s), 50 acoustic sub cycles were used for each simulation.

6

Conclusion

Through the discrete sampling of an analytic monopole source term, a quantification of the acoustic error was made as a function of the source term Courant number. By keeping the monopole constant at several values, the influence on the acoustic result when using disparate time scales between flow and acoustics was investigated. Keeping the monopole constant between source levels resembled a zeroth order interpolation between source levels. By varying the discretization of the source term, the degradation along the centerline of the domain could be quantified. Compared to a solution, which nearly resembled the analytic solution based on Green's function, the degradation increased most when the source term Courant number exceeded one.

In the next phase of the research the discretized monopole was used to test both the effect of interpolation at the node locations and by implementation of a higher order time integration method, which is called the spectral deferred correction (SDC) method. A combination of the higher order temporal precision of the source term calculation and the use of non-uniform nodes in the Lagrange interpolation causes the most accurate result for larger numbers of time step disparity. Based on these results, it can also be noted that Lagrange interpolation has the largest relative effect on improvement of the accuracy of the acoustic results when compared to temporal integration. The acoustic error improved by multiple orders when implementing Lagrange interpolation.

As was stated a new time integration method was tested, which is called the spectral deferred correction method. This method was used to solve an ordinary differential equation, which was defined in such a way that the solution equals the temporal part of the monopole source term. The SDC method showed its theoretical order behaviour, when solving for the source term. The spectral deferred correction method also improved the acoustic results compared to the backward Euler (BE) method. However the acoustic error was in the same order of magnitude for SDC and BE whereas the error in the source term differed multiple orders. The computational effort, due to the extra sweeps, is thus significantly higher for a minor acoustic improvement. Furthermore the relation between the acoustic error and the fluid error was established. It showed that improvements in the flow result do not have a linear effect on the acoustic result.

Finally the SDC method was tested, by implementation in an LES (large eddy simulation) solver. The solver was used to find a fluid solution for the flow which is emanated through the mouthpiece of an air reed instrument. The results showed, that the SDC method reduced the error for a backward Euler step of $t = 1e-5s$. The order behaviour was not the same as for solving the ordinary differential equation in chapter 4. This could be explained by the fact that the cell-centered values of the velocity are used for constructing higher order source terms. This causes inconsistencies in the temporal discretization. Therefore it is proposed to test alternative correction methodologies in the segregated approach used in the PISO algorithm. The Lagrange interpolation of the flow results improved the acoustic result significantly. Based on the findings in this research it can thus be noted that the influence of the interpolation is the dominant factor in resolving changes in time scale between the acoustic solver and the flow solver. Furthermore it can be noted that the Lagrange interpolation of the flow

results showed specific improvement in areas where flow behaviour was highly unsteady. Here the acoustic gain was significant. It should be noted that when working with Lighthill's equation the results in the source region are not realistic as was discussed in Chapter 2. However for the point of showing the mathematical improvement of the Lagrange interpolation, this result is relevant. In the far field the difference in perturbed density between the reference solution, zeroth order interpolation (wich resembles a piecewise constant source term) and Lagrange interpolation was small. Therefore Lagrange interpolation is specifically useful for acoustic analogies that can calculate the acoustic variables in the source region, where the flow can be highly unsteady.

7

Recommendations

In this section some recommendations are given for future work. One of the main findings in this research is that the Lagrange interpolation of the source term at the Gauss Lobatto locations has a significant effect on the acoustic accuracy produced by hybrid methods. Higher order time integration at the node locations also has an influence on the acoustic result, but the acoustic accuracy improvement was less significant. Further research can thus be conducted by establishing the relative influence of the parameters contained in the source term. It can then be determined how the parameters relate to changes in the acoustic result. In order to accomplish such an overview different acoustic analogies can be assessed.

In the tests the sub stepping in the solver was implemented correctly. By implementation of Gauss Lobatto substepping, the solution could be stored at these nodes. Based on the fluid flow results at these locations an interpolation of the velocity could be made. Furthermore the SDC (spectral deferred correction) method was incorporated to find a higher order approximation in time at the nodes. A clear improvement could be found, by using the method to solve an ordinary differential equation. However by implementation in the LES (large eddy simulation) solver, the error convergence of the SDC method was different from the evaluation of an ordinary differential equation. A possible reason for this inconsistent temporal behaviour is the occurence of oscillations in the solution due to a collocated grid [27]. Further research can be conducted by investigating the Rhie Chow interpolation correction and what modifications can be made for finding a temporal consistent behaviour of the solver for implementation of the SDC method in OpenFOAM.

Furthermore the SDC method requires function evaluations at the nodes. These function evaluations should contain only spatial discretization terms for a consistent temporal formulation. However by using the PISO algorithm with a turbulent term in the momentum equation, the function evaluations were more challenging to be explicitly determined in order to make the method consistent in time. Therefore more research can be conducted in the implementation of an SDC method in a turbulent model.

The SDC method requires a left hand side function evaluation of the time step to determine the spectral integration vector for node to node integration. Due to the absence of a consistent explicit formulation of the function value the difference between consecutive velocity values has to be determined to find this value. Since at the first time step such data is not available a backward Euler step was firstly used to initialize the SDC solver. It is thus interesting to quantify the effect on the obtained accuracy of starting an SDC method with a low order first time step.

The SDC method does not increase an order with every sweep for unstable solutions as was shown in chapter 4. Accelerating the convergence of SDC methods is a current interesting topic of research [16]. In an aeroacoustic context an accelerated SDC method could prove to be useful to increase the efficiency of the source term calculation. This then increases the efficiency of the entire hybrid system.

Finally concerning the interpolation a more elaborate research can be done in filtering for a specific part of the frequency spectrum [4]. Sound can produce a multitude of frequencies and the interpolation can be modified to accommodate the filtering of certain tones. This then results in an improved interpolation for a specific frequency range.

Bibliography

[1] C. K. W. Tam, *Computational aeroacoustics: Issues and methods,* AIAA Journal **33**, 1788 (1995).

[2] G. Cunha and S. Redonnet, *On the signal degradation induced by the interpolation and the sampling rate reduction in aeroacoustics hybrid methods,* International Journal for Numerical Methods in Fluids **71**, 910 (2013).

[3] C. Bogey, C. Bailly, and D. Juvé, *Computation of flow noise using source terms in linearized euler's equations,* AIAA Journal **40** (2002).

[4] G. Geiser, D. Marinc, and W. Schröder, *Comparison of source reconstruction methods for hybrid aeroacoustic predictions,* International Journal of Aeroacoustics **12**, 639 (2013).

[5] M. J. Lighthill, *On sound generated aerodynamically i. general theory,* Proceedings of the Royal Society of London **211**, 564 (1952).

[6] *The interaction between a background flow and a fluid,* `https://www.comsol.com/multiphysics/aeroacoustics`, accessed: 2018-03-12.

[7] S. Glegg and W. Devenport, *Aeroacoustics for low Mach number Flows* (Academic Press, 2017).

[8] J. Delfs, *Lecture notes grundlagen der aeroakustik,* (2016).

[9] T. Colonius and S. K. Lele, *Computational aeroacoustics: progress on nonlinear problems of sound generation,* Progress in Aerospace Sciences **40**, 345 (2004).

[10] M. Miyamoto, Y. Ito, K. Takahashi, T. Takami, T. Kobayashi, A. Nishida, and M. Aoyagi, *Numerical study on sound vibration of an air-reed instrument with compressible les,* arXiv:1005.3413[physics.flu-dyn] (2010).

[11] W. C. P. van der Velden, J. T. Akhnoukh, and A. H. van Zuijlen, *Low-order finite-volume based Riemann solver for application to aeroacoustic problems,* Journal of Computational Acoustics **25** (2017).

[12] D. G. Simons, *Lecture slides ae4431 aircraft noise and emissions,* (2016).

[13] J. T. Ahknoukh, *Linear acoustic solver in OpenFOAM*, Master's thesis, Delft university of technology, the Netherlands (2015).

[14] C. Bailly and D. Juvé, *Numerical solution of acoustic propagation problems using linearized euler equations,* AIAA Journal **38** (2000).

[15] A. Dutt, L. Greengard, and V. Rokhlin, *Spectral deferred correction methods for ordinary differential equations,* BIT Numerical Mathematics **40**, 241 (2000).

[16] R. Speck, D. Ruprecht, M. Emmett, M. Minion, M. Bolten, and R. Krause, *A multi-level spectral deferred correction method,* BIT numerical mathematics **55**, 843 (2015).

[17] R. Klees and R. Dwight, *Applied numerical analysis,* (2013).

[18] M. L. Minion, *Semi-implicit spectral deferred correction methods for ordinary differential equations,* Communications in Mathematical Sciences **1**, 471 (2003).

[19] D. Blom, *Efficient numerical methods for partitioned fluid-structure interaction simulations*, Ph.D. thesis, Delft university of technology, the Netherlands (2017).

[20] C. T. Lynch, *The numerical acoustic and fluid flow analysis on a CT-scan derived upper airway model of a stridor patient*, Master's thesis, Delft university of technology, the Netherlands (2012).

[21] *Openfoam v5 user guide: 4.5 solution and algorithm control,* `https://cfd.direct/openfoam/user-guide/fvsolution/`, accessed: 2018-03-11.

[22] H. Jasak, *Error Analysis and Estimation for the Finite Volume Method with Applications to Fluid Flows*, Ph.D. thesis, Imperial College of Science, Technology and Medicine, London (1996).

[23] R. Issa, *Solution of the implicitly discretised fluid flow equations by operator-splitting,* Journal of Computational Physics **62**, 40 (1986).

[24] A. de O. S. Moraes, P. L. C. Lage, G. C. Cunha, and L. F. L. R. Silva, *Analysis of the non-orthogonality correction of finite volume discretization on unstructured meshes,* 22nd International Congress of Mechanical Engineering. Ribeirão Preto, SP, Brazil , 3518 (2013).

[25] W. Z. Shen, J. A. Michelsen, and J. N. Sørensen, *Improved rhie-chow interpolation for unsteady flow computations,* AIAA Journal **39**, 2406 (2001).

[26] T. Behrens, *Openfoam's basic solvers for linear systems of equations,* (2009).

[27] F. P. Kärrholm, *Rhie chow interpolation in openfoam,* (2006).